Analysis of Evolving Oil Spills in Full-Polarimetric and Hybrid-Polarity SAR

Martine M. Espeseth, Stine Skrunes, *Member, IEEE*, Cathleen E. Jones, *Member, IEEE*,
Camilla Brekke, *Member, IEEE*, Benjamin Holt, *Member, IEEE*,
and Anthony P. Doulgeris, *Member, IEEE*

***Abstract*— Oil spill detection using a time series of images acquired off Norway in June 2015 with the uninhabited aerial vehicle synthetic aperture radar is examined. The relative performance of a set of features derived from quad-polarization versus hybrid-polarity (HP) modes in detection of various types of slicks as they evolve on a high wind driven sea surface is evaluated. It is shown that the HP mode is comparable with the full-polarimetric mode in its ability to distinguish the various slicks from open water (OW) for challenging conditions of high winds (9–12 m/s), small release volumes (0.2–0.5 m^3), and during the period 0–9 h following release. The features that contain the cross-polarization component are better for distinguishing the various slicks from open water at later and more developed stages. Although these features are not available in the HP mode, we identify alternative features to achieve similar results. In addition, a clear correlation between the results of individual features and their dependence on particular components within the two-scale Bragg scattering theory is identified. The features that show poor detectability of the oil slicks are those that are independent of the small-scale roughness, while the features resulting in good separability were dependent on several factors in the two-scale Bragg scattering model. We conclude that the HP mode is a viable alternative for SAR-based oil spill detection and monitoring that provides comparable results to those from the quad-polarimetric SAR.**

***Index Terms*—Hybrid polarity (HP), NORSE2015, oil spill observation, synthetic aperture radar (SAR), time series, uninhabited aerial vehicle synthetic aperture radar (UAVSAR).**

I. INTRODUCTION

SPACEBORNE and airborne remote sensing instruments are the key tools for an operational oil pollution monitoring program. Spaceborne instruments offer the unique capabilities of large swath widths and for some satellite constellation missions improved temporal coverage. Aircraft surveillance flights are flexible and allow monitoring of evolving oil with time, as well as verifying the oil in some cases. In recent years, characterizing oil spills in the marine environment using the full-polarimetric (FP) synthetic aperture radar (SAR) has intensified (see, e.g., [1]–[4]). During the Deepwater Horizon accident, the National Aeronautics and Space Administration (NASA) uninhabited aerial vehicle synthetic aperture radar (UAVSAR) provided the valuable observations of the major oil spill with fine resolution and a system that has a low noise floor [5]. An analysis of the FP SAR acquisitions revealed a potential in retrieval of quantitative slick properties [1].

FP SAR systems provide a unique capability of measuring the complete scattering matrix and allow identification and extraction of the scattering properties within a given resolution cell. However, the FP SAR system comes at a cost, typically a smaller spatial coverage or reduced spatial resolution compared with the dual-polarization (DP) and single-polarization SAR modes. A DP SAR transmits in one polarization and receives in two polarization channels. The choice of polarization for the conventional linear–linear DP SAR systems is horizontal (H) or vertical (V) linear polarization on transmit, and the backscattered response is measured in the horizontal and vertical linearly polarized channels. The drawback of using a DP SAR system is the reduced polarimetric information compared with FP. Raney [6] suggested that changing the polarization of the transmitted wave to circular polarization (resulting in a circular–circular system) gave a simpler instrument and improved the quality of the radar measurements in terms of minimizing sensitivity to relative errors and crosstalk, straightforward calibration of the radar signals, and decreasing the on-board resource requirements. This mode was named hybrid-polarity (HP) or compact-polarimetric (CP) mode. In addition, the polarimetric information given in the HP (CP) mode is in some cases reported to be close to that of FP SARs (see, e.g., [7]–[10]). The HP mode belongs to the DP SAR group, with wider swath and equal spatial resolution or improved spatial resolution and equal swath compared with the conventional FP SARs.

There exist a few studies on oil spill detection related to the use of simulated HP UAVSAR data from the Deepwater Horizon in the Gulf of Mexico from 2010 (see, e.g., [11], [12]). Collins *et al.* [11] investigated the reconstruction of a pseudo-FP covariance matrix from simulated HP data and computed the oil-water mixing index suggested in [13]. Shirvany *et al.* [12] investigated some simulated HP features and analyzed the appearance of the oil in the Deepwater

---

Manuscript received February 6, 2017; accepted March 9, 2017. Date of publication April 25, 2017; date of current version June 22, 2017. This work was supported in part by the Jet Propulsion Laboratory, California Institute of Technology under contract with the National Aeronautics and Space Administration, in part by the Centre for Integrated Remote Sensing and Forecasting for Arctic Operations (CIRFA) under Research Council of Norway (RCN) Grant 237906, and in part by the NORRUSS Program under RCN under Grant 233896. *(Corresponding author: Martine M. Espeseth.)*

M. M. Espeseth, S. Skrunes, C. Brekke, and A. P. Doulgeris are with the Department of Physics and Technology, UiT The Arctic University of Norway, 9019 Tromsø, Norway (e-mail: martine.espeseth@uit.no; stine.skrunes@uit.no; camilla.brekke@uit.no; anthony.p.doulgeris@uit.no).

C. E. Jones and B. Holt are with the Jet Propulsion Laboratory, California Institute of Technology, Pasadena, CA 91125 USA (e-mail: cathleen.e.jones@jpl.nasa.gov; benjamin.m.holt@jpl.nasa.gov).

Color versions of one or more of the figures in this paper are available online at http://ieeexplore.ieee.org.

Digital Object Identifier 10.1109/TGRS.2017.2690001

$$\sigma^0_{\mathrm{HH}} = 4\pi k_r^4 \cos^4(\theta_i) \left| \left(\frac{\sin(\theta+\psi)\cos(\xi)}{\sin(\theta_i)}\right)^2 R_{\mathrm{HH}}(\theta_i, \epsilon_r) + \left(\frac{\sin(\xi)}{\sin(\theta_i)}\right)^2 R_{\mathrm{VV}}(\theta_i, \epsilon_r)\right|^2 W(2k_r \sin(\theta+\psi), 2k_r \cos(\theta+\psi)\sin(\xi)) \quad (1)$$

$$\sigma^0_{\mathrm{VV}} = 4\pi k_r^4 \cos^4(\theta_i) \left| \left(\frac{\sin(\theta+\psi)\cos(\xi)}{\sin\theta_i}\right)^2 R_{\mathrm{VV}}(\theta_i, \epsilon_r) + \left(\frac{\sin(\xi)}{\sin(\theta_i)}\right)^2 R_{\mathrm{HH}}(\theta_i, \epsilon_r)\right|^2 W(2k_r \sin(\theta+\psi), 2k_r \cos(\theta+\psi)\sin(\xi)) \quad (2)$$

$$\sigma^0_{\mathrm{HV}} = 4\pi k_r^4 \cos^4(\theta_i) \left(\frac{\sin(\theta+\psi)\cos(\xi)\sin(\xi)}{\sin^2(\theta_i)}\right)^2 |R_{\mathrm{VV}}(\theta_i, \epsilon_r) - R_{\mathrm{HH}}(\theta_i, \epsilon_r)|^2 W(2k_r \sin(\theta+\psi), 2k_r \cos(\theta+\psi)\sin(\xi)) \quad (3)$$

Horizon slick using one UAVSAR scene covering a relatively thick oil slick under low wind conditions.

The backscattered response from clean seas and oil slicks within SAR scenes is complex and dependent on several factors, including amongst others the slick characteristics (dielectric properties, viscosity, extent, and composition), environmental conditions (wind, sea state, and temperature), and sensor properties [frequency, resolution, coverage, and signal-to-noise ratio (SNR)]. In general, oil spills will spread to form a thin layer on the water surface, and this layer will dampen the small-scale roughness on the ocean surface, resulting in reduced backscattered power [14]. Another factor that can reduce the backscattered power is a reduction in the dielectric constant within the slick compared with the clean sea. This factor will contribute to the detectability if the oil slick is thick enough and/or the concentration of the oil droplets within the water column is high enough [13]. The backscattering of microwaves from a clean sea surface is usually described using the Bragg scattering theory, in which the incoming wave is in resonance with the ocean waves (resonant scattering) [15], [16]. The Bragg waves can further be modulated by the longer waves on which they ride through tilt and hydrodynamic effects [17].

For the first time, in this paper, we investigate the difference between FP and HP for a series of UAVSAR scenes covering various types of oil slicks under high wind condition as they evolve following release. This paper investigates and compares FP and simulated HP data acquired over slicks using a unique UAVSAR time series acquired in the FP mode. The UAVSAR time series was collected from a controlled oil spill experiment, the NOrwegian Radar oil Spill Experiment 2015 (NORSE2015), that took place in the North Sea at the Frigg field in June 2015. This experiment was a collaboration between UiT The Arctic University of Norway, the Jet Propulsion Laboratory (JPL)/NASA, and the Norwegian Clean Seas Association for Operating Companies. The UAVSAR time series was collected during two flights during a single day with approximately 3 h between the end of data acquisition in the first and the beginning of data acquisition in the second. There were 16 and 6 acquisitions in the first and second flights, respectively, obtained over an 8-h total time span. The UAVSAR was used to image four different oil slicks as they evolved and weathered on a high wind sea surface (approximately 12 m/s). In addition, X-, C-, and L-band SAR data were also collected from satellite SAR sensors coincident with one of the UAVSAR images. The reader is referred to [18]–[20] for additional information and analysis from the experiment.

The main objectives of this paper are: 1) to study the performance of a set of well-known FP and HP features to detect oil slicks; 2) to identify and compare the best FP and HP features for detecting the evolving oil slicks; 3) to identify the dominating components in the Bragg scattering theory to which the investigated FP and HP polarimetric features are sensitive; and 4) to study the difference in detectability of the various oil slicks as they developed.

The Bragg scattering theory and the HP theory are described in Section II, the experiment is described in Section III, the preprocessing steps are described in Section IV and in the Appendix, and Section V contains the information about the polarimetric features used in this paper. Section VI presents the time series results, and Section VII presents the conclusions of this paper.

II. THEORY

In this section, we introduce the tilted Bragg scattering model used for the FP data, the theory of the HP SAR mode, and the two-scale Bragg model that is adapted for the HP mode.

A. Tilted Bragg Model

The backscatter from the ocean surface can be described through the theory of Bragg. Bragg scattering is caused by small-scale surface roughness whose height is small compared with the radar wavelength [15]. In addition, the in-plane tilt and the out-of-plane tilt of the facet, caused by the large-scale gravity waves on the ocean surface, will alter a response in the like-polarized channel and add a response in the cross-polarized channel. Including this tilt of the surface in the Bragg model leads to the tilted Bragg model (also known as the Valenzuela model) [15]. From this model, the equations of the normalized radar cross sections from an FP SAR system are given in (1)–(3), as shown at the top of the page. In these equations, k_r is the wavenumber, θ is the incidence angle relative to the untilted horizontal plane [1], and $\theta_i = \cos^{-1}[\cos(\theta+\psi)\cos(\xi)]$ is the local incidence angle. ψ is the angle between the vertical and the normal to the patch projected into the plane of incidence, and ξ is the angle between the vertical and the normal to the patch projected into the plane perpendicular to the plane of incidence [15]. $W(\cdot)$ is the 2-D wavenumber spectral density of the ocean surface roughness, and R_{HH} and R_{VV} are the Bragg scattering coefficients defined as [1]

$$R_{\mathrm{HH}}(\theta_i, \epsilon_r) = \frac{\cos(\theta_i) - \sqrt{\epsilon_r - \sin^2(\theta_i)}}{\cos(\theta_i) + \sqrt{\epsilon_r - \sin^2(\theta_i)}} \quad (4)$$

and

$$R_{\mathrm{VV}}(\theta_i, \epsilon_r) = \frac{(\epsilon_r - 1)(\sin^2(\theta_i) - \epsilon_r(1 + \sin^2(\theta_i)))}{(\epsilon_r \cos(\theta_i) + \sqrt{\epsilon_r - \sin^2(\theta_i)})^2} \tag{5}$$

where ϵ_r is the relative dielectric constant, and the subscripts of R_{HH} and R_{VV} represent the transmit and the receive polarizations. As can be observed from (4) and (5), the backscattered radar cross sections are dependent on several components, namely, the wave spectrum, the imaging geometry, and the dielectric properties of the media.

B. Hybrid-Polarity Theory

In this paper, we investigate the HP system with right circular transmit and linear receive architecture. This configuration is already integrated in current satellite missions, such as RISAT-1 and ALOS-2, and will also be incorporated in several upcoming spaceborne SARs. Recognizing its great potential for oil spill detection identified in [10] and [11], we choose HP as a comparing system to FP SAR in this paper. The fundamental quantities measured by a polarimetric SAR system are the complex backscattering terms S_{ij}. Here, i and j define the polarizations of the transmit and receive channels in the radar system. The HP mode transmits only one circular polarization, either left (L) or right (R), and receives two orthogonal linear polarizations, namely, horizontal and vertical [6]. For the right circular HP mode, the scattering vector is defined as

$$\bar{k}_{(\mathrm{RH},\mathrm{RV})} = [S_{\mathrm{RH}}, S_{\mathrm{RV}}]^T \tag{6}$$

where T denotes the transpose operator. The right circularly polarized transmit mode is used throughout this paper. In the linear horizontal and vertical basis, the scattering vector is expressed as [21]

$$\bar{k}_{(\mathrm{RH},\mathrm{RV})} = \frac{1}{\sqrt{2}}[S_{\mathrm{HH}} - iS_{\mathrm{HV}}, -iS_{\mathrm{VV}} + S_{\mathrm{HV}}]^T \tag{7}$$

where reciprocity is assumed ($S_{\mathrm{HV}} = S_{\mathrm{VH}}$). The UAVSAR instrument is an FP radar, and the HP scattering vector is simulated based on (7). In the FP SAR data, we have both co- and cross-polarized channels. By looking at the scattering vector $\bar{k}_{(\mathrm{RH},\mathrm{RV})}$, we can observe that the co- and cross-polarized components are not possible to isolate, since the HP scattering components are a mix of co- and cross-polarized terms. Combining the two measured linear horizontal and vertical polarization values, we can also form orthogonal components in the circular–circular polarization basis as [22]

$$\begin{aligned}\bar{k}_{(\mathrm{RR},\mathrm{RL})} &= [S_{\mathrm{RR}}, S_{\mathrm{RL}}]^T \\ &= \frac{1}{\sqrt{2}}[-S_{\mathrm{RH}} + iS_{\mathrm{RV}}, iS_{\mathrm{RH}} - S_{\mathrm{RV}}]^T \\ &= \frac{1}{2}[S_{\mathrm{VV}} - S_{\mathrm{HH}} + 2iS_{\mathrm{HV}}, i(S_{\mathrm{HH}} + S_{\mathrm{VV}})]^T.\end{aligned} \tag{8}$$

The expected sense of received circular polarization is opposite to the transmitted sense [23]. Therefore, S_{RR} becomes the cross-polarization state, while S_{RL} is the like-polarization state [23]. This corresponds to the CP SAR group, where the antenna transmits on right circular and receives in both right-hand circular and left-hand circular. Note, our initial starting point is still a simulated HP SAR system, but the HP scattering vector is in this case projected onto the circular basis at the receiver. Polarimetric features extracted from $\bar{k}_{(\mathrm{RH},\mathrm{RV})}$ and $\bar{k}_{(\mathrm{RR},\mathrm{RL})}$ will in Sections V and VI be investigated.

The polarimetric sample covariance matrix can be calculated from the target vector for each polarimetric system. The sample FP covariance matrix is given as

$$\boldsymbol{C}_{\mathrm{FP}} = \frac{1}{L}\sum_{j=1}^{L} \bar{k}_{\{j,(\mathrm{FP})\}}\bar{k}^{\star T}_{\{j,(\mathrm{FP})\}} \tag{9}$$

where $\star$ represents complex conjugate, $\bar{k}_j$ is the jth lexicographic scattering vector $\bar{k}_j = [S_{\mathrm{HH}}, S_{\mathrm{HV}}, S_{\mathrm{VH}}, S_{\mathrm{VV}}]^T$, and L is the number of samples included in the computation of the covariance matrix (the number of looks). Similarly, the sample HP covariance matrices in the circular–linear and circular–circular basis are given as

$$\boldsymbol{C}_{(\mathrm{RH},\mathrm{RV})} = \frac{1}{L}\sum_{j=1}^{L} \bar{k}_{\{j,(\mathrm{RH},\mathrm{RV})\}}\bar{k}^{\star T}_{\{j,(\mathrm{RH},\mathrm{RV})\}} \tag{10}$$

and

$$\boldsymbol{C}_{(\mathrm{RR},\mathrm{RL})} = \frac{1}{L}\sum_{j=1}^{L} \bar{k}_{\{j,(\mathrm{RR},\mathrm{RL})\}}\bar{k}^{\star T}_{\{j,(\mathrm{RR},\mathrm{RL})\}}. \tag{11}$$

Several studies have attempted to reconstruct a pseudo-FP covariance matrix, i.e., transforming from (10) to (9) (see, e.g., [21]–[24]). To do so, it is necessary to make some assumptions about the backscattering properties. As highlighted in [25], the appropriate methodology is to directly compare the HP with the FP mode without transforming to a pseudo-FP covariance matrix, thus avoiding any assumptions. In this paper, we follow Raney's methodology [25] and perform the study on features extracted directly from the simulated HP data. It is important to be aware that the use of HP mode in the UAVSAR instrument will not increase the swath width due to the design of the system. Also, when simulating the HP data from the FP data, a 3-dB power loss is introduced due to $\sqrt{2}$ in (7) [8].

Only the radar cross section of the HH, HV, and VV channels are estimated in the tilted Bragg model discussed in Section II-A. In order to have model estimates of the HP data, another model containing the complex backscattering coefficients is needed. In addition, a similar model is also necessary when evaluating polarimetric features from the FP covariance matrix. Therefore, Salberg *et al.* [10] suggested to use the two-scale Bragg for the HP mode. This model is similar to the tilted Bragg model in terms of containing two scales of the surface roughness, namely, the small- and the large-scale roughness. Salberg *et al.* [10] used the two-scale model by first simulating the HP scattering vector followed by a projection to the circular basis. The matrix ($\boldsymbol{S}$) of scattering coefficients denotes the Sinclair scattering matrix. Following the two-scale model, $\boldsymbol{S}$ can be expressed as [10], [26]:

$$\boldsymbol{S} = a_s\boldsymbol{R}(\phi)\begin{bmatrix} R_{\mathrm{HH}}(\theta_i, \epsilon_r) & 0 \\ 0 & R_{\mathrm{VV}}(\theta_i, \epsilon_r)\end{bmatrix}\boldsymbol{R}^T(\phi) \tag{12}$$

where $|a_s|^2 = k_r^4 \cos^4(\theta_i) W(\cdot)$ contains the factors related to the small-scale roughness, such as the ocean wave spectrum, incidence angle, and wavenumber. The rotation matrix $\boldsymbol{R}(\phi)$ is given as

$$\boldsymbol{R}(\phi) = \begin{bmatrix} \cos(\phi) & \sin(\phi) \\ -\sin(\phi) & \cos(\phi) \end{bmatrix}. \tag{13}$$

The tilt of the facet causes a rotation of the local plane of incidence around the look direction by an angle ϕ [27]. $\boldsymbol{R}(\phi)$ depends on the surface slope (azimuth and range directions) or large-scale roughness and the radar look angle [22], [27]. Calculating the expression in (12) gives (14), as shown at the bottom of the page. Inserting (14) into (7) gives (15), as shown at the bottom of the page. Both S_{RH} and S_{RV} depend on the rotation angle (ϕ), so Salberg *et al.* [10] suggested to consider the following quantities:

$$\begin{aligned} S_{\mathrm{RH}} - iS_{\mathrm{RV}} &= \frac{1}{\sqrt{2}}(S_{\mathrm{HH}} - S_{\mathrm{VV}} - 2iS_{\mathrm{HV}}) \\ &= \frac{a_s}{\sqrt{2}}(R_{\mathrm{HH}}(\theta_i, \epsilon_r) - R_{\mathrm{VV}}(\theta_i, \epsilon_r)) \exp(2\phi i) \\ S_{\mathrm{RH}} + iS_{\mathrm{RV}} &= \frac{1}{\sqrt{2}}(S_{\mathrm{HH}} + S_{\mathrm{VV}}) \\ &= \frac{a_s}{\sqrt{2}}(R_{\mathrm{HH}}(\theta_i, \epsilon_r) + R_{\mathrm{VV}}(\theta_i, \epsilon_r)). \end{aligned} \tag{16}$$

Note the similarity to (8), where the

$$\begin{aligned} \bar{k}_{(\mathrm{RR,RL})} &= \begin{bmatrix} S_{\mathrm{RR}} \\ S_{\mathrm{RL}} \end{bmatrix} = \frac{1}{\sqrt{2}} \begin{bmatrix} -(S_{\mathrm{RH}} - iS_{\mathrm{RV}}) \\ i(S_{\mathrm{RH}} + iS_{\mathrm{RV}}) \end{bmatrix} \\ &= \frac{a_s}{2} \begin{bmatrix} (R_{\mathrm{VV}}(\theta_i, \epsilon_r) - R_{\mathrm{HH}}(\theta_i, \epsilon_r)) \exp(2\phi i) \\ i(R_{\mathrm{HH}}(\theta_i, \epsilon_r) + R_{\mathrm{VV}}(\theta_i, \epsilon_r)) \end{bmatrix}. \end{aligned} \tag{17}$$

The intensity of S_{RR} and S_{RL} becomes

$$\begin{aligned} |S_{\mathrm{RR}}|^2 &= \left| -\frac{1}{\sqrt{2}}(S_{\mathrm{RH}} - iS_{\mathrm{RV}}) \right|^2 \\ &= \frac{|a_s|^2}{4} |R_{\mathrm{VV}}(\theta_i, \epsilon_r) - R_{\mathrm{HH}}(\theta_i, \epsilon_r)|^2 \end{aligned} \tag{18}$$

and

$$\begin{aligned} |S_{\mathrm{RL}}|^2 &= \left| \frac{i}{\sqrt{2}}(S_{\mathrm{RH}} + iS_{\mathrm{RV}}) \right|^2 \\ &= \frac{|a_s|^2}{4} |R_{\mathrm{HH}}(\theta_i, \epsilon_r) + R_{\mathrm{VV}}(\theta_i, \epsilon_r)|^2. \end{aligned} \tag{19}$$

We observe that S_{RL} is independent of the rotation angle and so are $|S_{\mathrm{RR}}|^2$ and $|S_{\mathrm{RL}}|^2$. Note, however, that all of these include the Bragg coefficients, which are dependent on the tilt angles. The theory of tilted Bragg and the two-scale Bragg models will be used as a fundamental theory both when presenting the polarimetric features investigated and when evaluating the results from the UAVSAR data (Sections V and VI).

TABLE I

PROPERTIES OF THE EXPERIMENTAL OIL RELEASES DURING NORSE2015 [18], [19]

Release	Time (UTC)	Substance	Volume
PO	04:48	Plant Oil: Radiagreen ebo	0.2 m^3
E40	04:59	Emulsion (40% oil) 300 L water + 100 L Troll + 100 L Oseberg + 0.2 L One-Mul	0.5 m^3
E60	05:15	Emulsion (60% oil) 200 L water + 150 L Troll 150 L Oseberg + 0.2 L One-Mul	0.5 m^3
E80	05:30	Emulsion (80% oil) 100 L water + 200 L Troll + 200 L Oseberg + 0.2 L One-Mul	0.5 m^3

III. NORSE2015 EXPERIMENT

An extensive SAR data set was collected from both the airborne and spaceborne platforms during the NORSE2015 experiment at the abandoned Frigg field in the North Sea. *In situ* data, including wind, temperature, and oil-to-water ratios of the released oils, were collected and have been described in detail previously [18], [19]. The main motivation behind the NORSE2015 experiment was to collect the multisensor and multifrequency SAR data to study the polarization-dependent electromagnetic signals and their relationship to varying oil–water mixtures and dielectric properties, as well as study the evolving oil slicks' drift and characteristics as a function of time using SAR [18]–[20], [28], [29]. Table I summarizes the information about the released oil, which was three emulsions based on the same crude oil but with different volumetric oil concentrations, i.e., 40% oil (E40), 60% oil (E60), 80% oil (E80), and release of plant oil (PO) for the simulation of a natural biogenic slick.

The VV-intensity images for the UAVSAR scenes are shown in Fig. 1. These intensity images are geocoded, smoothed, and scaled for displaying purposes, and the ships are masked out and colored red. Note that the true width (number of pixels in the subsection displayed) of the images varies across the time series as the oil slicks evolve and spread out. The release of the E80 slick was not complete in the first UAVSAR acquisition, so this scene is not used in the analysis of the E80 slick. The PO and the three emulsion slicks are shown in Fig. 1, with the PO as the southern-most slick, and E40, E60, and E80 to the north. The properties of the UAVSAR sensor are given in Table II.

The oils were released along a line approximately parallel to the spaceborne SAR flight directions to obtain similar incidence angles for all slicks. In order to maximize the SNRs, the releases were done close to the center of the swaths. The UAVSAR acquisitions were then adapted to this setup

---

$$\boldsymbol{S} = \begin{bmatrix} S_{\mathrm{HH}} & S_{\mathrm{HV}} \\ S_{\mathrm{HV}} & S_{\mathrm{VV}} \end{bmatrix} = a_s \begin{bmatrix} R_{\mathrm{HH}}(\theta_i, \epsilon_r)\cos^2(\phi) + R_{\mathrm{VV}}(\theta_i, \epsilon_r)\sin^2\phi & \cos(\phi)\sin(\phi)(R_{\mathrm{VV}}(\theta_i, \epsilon_r) - R_{\mathrm{HH}}(\theta_i, \epsilon_r)) \\ \cos(\phi)\sin(\phi)(R_{\mathrm{VV}}(\theta_i, \epsilon_r) - R_{\mathrm{HH}}(\theta_i, \epsilon_r)) & R_{\mathrm{VV}}(\theta_i, \epsilon_r)\cos^2(\phi) + R_{\mathrm{HH}}(\theta_i, \epsilon_r)\sin^2\phi \end{bmatrix} \tag{14}$$

$$\bar{k}_{(\mathrm{RH,RV})} = \begin{bmatrix} S_{\mathrm{RH}} \\ S_{\mathrm{RV}} \end{bmatrix} = \frac{a_s}{\sqrt{2}} \begin{bmatrix} R_{\mathrm{HH}}(\theta_i, \epsilon_r)\cos^2(\phi) + R_{\mathrm{VV}}(\theta_i, \epsilon_r)\sin^2(\phi) + i(\cos(\phi)\sin(\phi)(R_{\mathrm{HH}}(\theta_i, \epsilon_r) - R_{\mathrm{VV}}(\theta_i, \epsilon_r))) \\ \cos(\phi)\sin(\phi)(R_{\mathrm{VV}}(\theta_i, \epsilon_r) - R_{\mathrm{HH}}(\theta_i, \epsilon_r)) - i(R_{\mathrm{HH}}(\theta_i, \epsilon_r)\sin^2(\phi) + R_{\mathrm{VV}}(\theta_i, \epsilon_r)\cos^2\phi) \end{bmatrix} \tag{15}$$

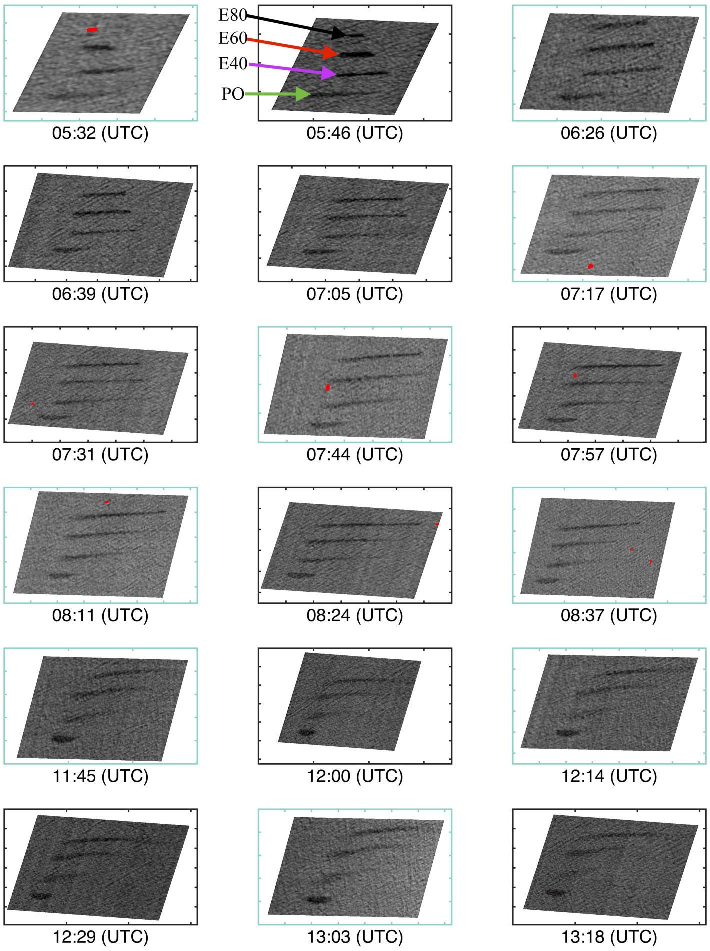

05:32 (UTC) 05:46 (UTC) 06:26 (UTC)
06:39 (UTC) 07:05 (UTC) 07:17 (UTC)
07:31 (UTC) 07:44 (UTC) 07:57 (UTC)
08:11 (UTC) 08:24 (UTC) 08:37 (UTC)
11:45 (UTC) 12:00 (UTC) 12:14 (UTC)
12:29 (UTC) 13:03 (UTC) 13:18 (UTC)

Fig. 1. Geocoded VV-intensity for the ascending (blue box) and descending (black box) UAVSAR scenes. The images are oriented with north pointing upward, and the ships are masked out and colored red. UAVSAR data are the courtesy of NASA/JPL-Caltech.

TABLE II

PROPERTIES OF THE UAVSAR SENSOR [5] AND THE UAVSAR SLC DATA PRODUCTS FOR THE ACQUIRED TIME SERIES OF IMAGES

Date	Time[a] (UTC)	Mode	Polarization	Frequency [GHz]	Incidence angle	NESZ [dB]	Resolution (rg[b] × az[c])	Swath width	Look direction
10th June 2015	05:32 - 13:18	PolSAR	Full-pol (HH,HV,VH,VV)	L-band (1.26)	19.5° to 67.5°	∼ -48 to -33	2.5 m × 1 m	20 km	Left

[a]Time when starting the acquisition to the end of the acquisition (including both flight 1 and 2), [b]rg: range, [c]az: azimuth

and the research team onboard the aircraft selected the flight lines so that the oil slicks were located where the antenna gain was near its maxima. The noise floor as a function of incidence angle (along the range direction) is shown for the UAVSAR instrument in [5, Fig. 1]. Here, the minimum noise is found near mid-swath in the range direction. Fig. 2 shows the incidence angle span for each slick along the UAVSAR time series. The UAVSAR monitored the evolving slicks in three different look directions and five different imaging geometries. In order to limit the effect from the imaging geometry on the polarimetric features, only ID numbers 00709 (ascending) and 18709 (descending) are used in this paper, with white background in Fig. 2. This is because these two data sets of imaging geometries contain the most scenes and the oil slicks are located at approximately the same incidence angles across the two subsets. The gray background denotes the scenes that are left out of this analysis and are the ones with slightly different imaging geometries. However, these scenes will be included in a future study that analyzes the effects from the imaging geometry on several polarimetric features.

IV. PREPROCESSING

In this section, we introduce the separability measure that is used when evaluating the performance in the preprocessing steps and the different polarimetric features. Furthermore, we discuss each of the steps that are performed on the UAVSAR data prior to the polarimetric analysis.

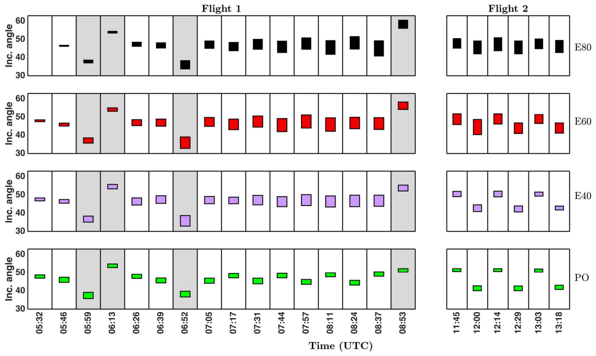

Fig. 2. Overview of the incidence angle range for each slick along the UAVSAR time series. The white colored sections (a total of 18 UAVSAR scenes) are used in this analysis, and the gray colored sections are not included.

A. Separability Measure

In this paper, several polarimetric features are compared in terms of how well they separate the various oil slicks from each other as well as from open water (OW). In the literature, several statistical metrics are described that can be used to accomplish this task. We want to use a statistical distance measure that can be applied across the UAVSAR time series for the range of polarimetric features investigated. The Bhattacharyya distance in the closed-form expression [30] has been used in [10] for evaluating the separability between various oil slicks and open water using some selected polarimetric features. Similarly, the normalized distance between the means was used in [31]. Evaluating the mean and standard deviations for each polarimetric feature relative to each other has been done in several studies (see, e.g., [3], [32]). In our case, we choose to use a distance measure that captures both the mean and the standard deviation of the polarimetric feature and, at the same time, is defined on an interval with discrete boundaries. We use the closed-form expression of the Bhattacharyya distance and assume Gaussian distributed data. This distance measure is defined as [30]

$$d_{ij} = \frac{1}{4}(\mu_j - \mu_i)^T\left(\Sigma_i^{-1} + \Sigma_j^{-1}\right)(\mu_j - \mu_i) + \frac{1}{2}\log\left(\frac{|\Sigma_i + \Sigma_j|}{2\sqrt{|\Sigma_i \Sigma_j|}}\right) \qquad (20)$$

where μ_i and μ_j are the mean values and Σ_i and Σ_j denote the covariance matrices of the classes i and j, respectively. Superscript T denotes the transpose operator. In this paper, we apply this measure to each of the 1-D polarimetric features, i.e., Σ_i is the marginal variance and the transpose operator is not necessary. This distance spans from 0 (high similarity) to infinity (low similarity). To obtain a distance measure with discrete boundaries, we apply the Jeffries–Matusita (JM) distance, which takes values in the interval 0 (high similarity) to 2 (low similarity) [33]. The JM distance is defined as [33], [34]

$$\mathrm{JM}_{ij} = 2(1 - e^{-d_{ij}}) \qquad (21)$$

where d_{ij} is the Bhattacharyya distance given in (20). The JM_{ij} distance is well described in [33], and has been used for the sea ice classification in SAR data [35]. This measure is a function of the mean and standard deviation between feature values representing two given classes in our case the various oil slicks and open water. Dabboor and Geldsetzer [35] defined a JM of ≥ 1 to indicate that two classes are considered to be separable. Fig. 3 shows the examples on the sensitivity of the JM distance, where the histograms of four slicks and open water regions and their corresponding intensity images are displayed. We note that the boundary around the edges of the slick is partially composed of both oil and water, and the pixels will therefore be a mix of these. In two of the examples in Fig. 3, the JM distance is slightly above 0.8. These slicks are visible from the surrounding clean sea, and we therefore define JM values to be "acceptable" at a threshold of 0.8 and "confident" at 1.

B. Speckle Filtering

The backscattered signals from the surface can interfere constructively or destructively to produce bright and dark pixels in the SAR scene, known as speckle variation. Prior to calculating the polarimetric features used in this paper, speckle filtering is performed using a box-car filter. Following the selection of the filter, we select the window size (also known as the number of looks). The choice of number of looks has a great impact on the spatial resolution and on the contrast between the oil slicks and the clean sea. With the high resolution of the UAVSAR scenes, we can afford to have a coarser resolution with the gain of reducing speckle. The UAVSAR ground range resolution is 2.5 m (the slant range resolution is 1.7 m) and the azimuth resolution is 1 m [1], [5]. In the multilooking process, Minchew *et al.* [1] chose the relation to be one to four between the looks in the range and azimuth directions. We apply the same relation in this analysis when multilooking the data. Additionally, to achieve a good compromise between speckle reduction and preservation of details, a sliding window is used in the feature computations.

The single-look complex (SLC) images are smoothed with a mask of 15 × 60 pixels (range × azimuth). Fig. 4 shows the effect of smoothing on the JM separability of the VV-damping ratio between open water and between the four slicks as the total number of looks (both in range and azimuth) increases. The effect of increasing the number of looks in the averaging process is significant for all the JM distances of the four slicks and open water. In this case, we show the effect on two scenes, but similar results have been obtained for the other scenes as well. It is already known that increasing the mask size will enhance interpretability [36], but the small oil slicks might hamper detectability. From Fig. 4, the minimum mask size for separating the four slicks from the open water varies depending on the oil type. For these two scenes, less averaging is necessary to separate the PO from the open water compared to separating the emulsion slicks from the open water regions. Less averaging is needed for the E80 followed by E60 and E40. Because our main goal is to study the

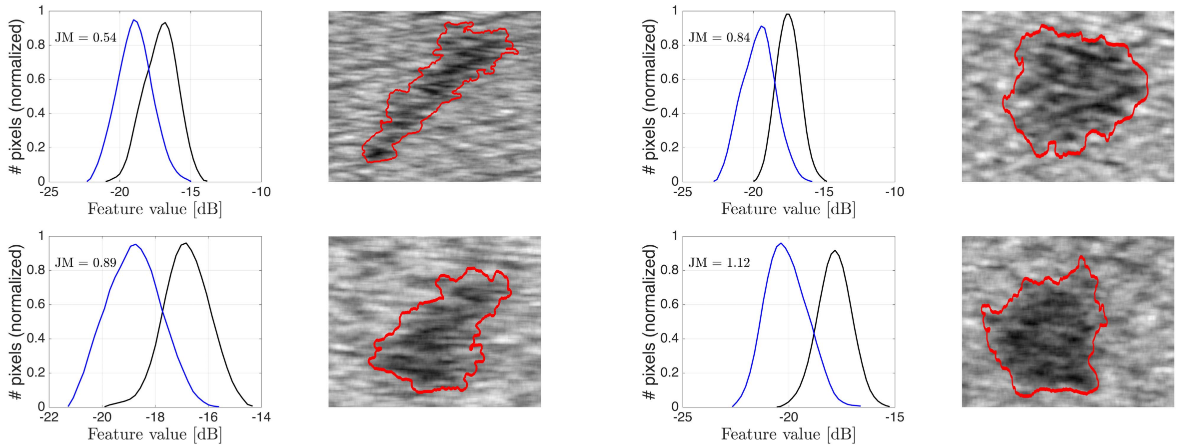

Fig. 3. Sensitivity of various values of the JM distance using the VV-intensity is illustrated using the histograms of the VV-intensity of four oil slicks (black color) and open water (blue color) with the same incidence angle range. The JM distance is calculated between the oil slick region and the open water region. Intensity images with the outline of the segmented masks are given to the right of their corresponding histograms.

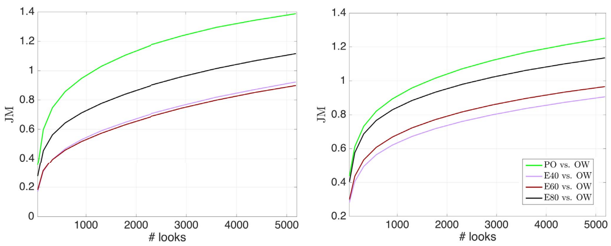

Fig. 4. Effect of increasing the number of looks in the speckle filtering on the JM separability between the four slicks and the open water using the VV-damping ratio. (Left) UAVSAR acquisition taken at 07:17 UTC. (Right) Scene acquired at 07:44 UTC.

evolution of different oil slicks, it is important to enhance interpretability of the oil slicks and, at the same time, keep a high spatial resolution.

C. Segmentation

Our goal is to evaluate the detectability of several polarimetric features for the various slick types over the UAVSAR time series. To be able to compare detectability, we need to segment out the different slicks. The same segmentation method should be applied on each scene for consistency and to avoid errors introduced by manual selection. Several segmentation methods for oil spill detection have already been extensively studied in the literature (see, e.g., [37], [38]). In our case, we choose a method that is generic and relatively simple to use, namely, the "extended polarimetric feature space" (EPFS) unsupervised method described in [39] and [40]. This unsupervised segmentation method includes both the polarimetric information and the textural information from the SAR data and groups all pixels with similar statistical properties in the same clusters.

The intensity variation related to incidence angle can be larger than the intensity difference between the classes, and hence, the oil slicks might be neglected in the original segmentation. Furthermore, the oil slicks spread out in the range direction with time, increasing the incidence angle span across the slicks. Therefore, an incidence angle correction (described in the Appendix) is applied on the scattering vector prior to segmentation.

The EPFS method can be split into four stages. The first is extraction of input features from the SAR data. Here, we use the span and the relative kurtosis [40] as an input. This stage also includes transforming the extracted features to partially remove non-Gaussian spreading and improve symmetry of the clusters, which is often achieved with the log operator. The second stage is to subsample the input features to speed up the segmentation process. In the third stage, the clusters are created using the expectation–maximization (EM) algorithm, assuming a multivariate Gaussian model for the transformed features. The number of classes (clusters) is usually a necessary input choice when segmenting, but this approach instead automatically determines the number of clusters using a goodness-of-fit test stage and sequentially applies the EM algorithm. Finally, a discrete Markov random field contextual smoothing stage completes the segmentation by integrating contextual information to improve the connectivity within the image segments. After the unsupervised segmentation approach, the oil slick regions are manually chosen from the output segments and labeled based on the *in situ* data.

Fig. 5 shows the segmentation results for the different slicks in the UAVSAR acquisition at 06:26 UTC. The green mask is PO, pink is E40, red is E60, and black is E80. Several open water regions are selected to determine the variance in the clean water properties and to enable a reasonable representation of the polarimetric features representing the open water class under the same environmental conditions as the slicks. These are selected based on the same shape for each slick, as shown in Fig. 5. This is done in order to have an equal number of open water samples as the oil slick as well as an equal number of pixels in both the range and azimuth directions, which matches the incidence angles of the slick pixels.

TABLE III

OVERVIEW OF THE INVESTIGATED FP POLARIMETRIC FEATURES (COMPUTED USING A MASK OF 15 × 60 PIXELS). THE REFERENCES INCLUDED ARE THE EXAMPLES OF STUDIES WHERE THE FEATURES HAVE BEEN STUDIED FOR OIL SPILL OBSERVATION

FP Features	
Name	Formula
Damping ratio ([1] [3] [41] [42])	$\zeta_{ij} = 10 \log_{10}\left(\frac{\langle I_{ij}^{(sea)}\rangle}{\langle I_{ij}^{(slick)}\rangle}\right), I_{ij} = \lvert S_{ij}\rvert^2$ $(i, j) \in \{(\mathrm{H,H}) \vee (\mathrm{H,V}) \vee (\mathrm{V,H}) \vee (\mathrm{V,V})\}$
Copolarization power ratio ([1] [2])	$\gamma_{CO} = \frac{\langle I_{VV}\rangle}{\langle I_{HH}\rangle}$
Real and imaginary part of the copolarization cross product ([2] [3] [19])	$r_{CO} = \lvert\Re(\langle S_{HH}S^{\star}_{VV}\rangle)\rvert, i_{CO} = \lvert\Im(\langle S_{HH}S^{\star}_{VV}\rangle)\rvert$
Standard deviation of the copolarization phase difference ([4] [43])	$\phi_{CO} = \sqrt{\langle(\phi_{HH} - \phi_{VV})^2\rangle + (\langle\phi_{HH} - \phi_{VV}\rangle)^2}$
Magnitude of the copolarization correlation coefficient ([2] [9] [44] [45] [44])	$\rho_{CO} = \frac{\lvert(S_{HH}S^{\star}_{VV})\rvert}{\sqrt{\langle\lvert S_{HH}\rvert^2\rangle\langle\lvert S_{VV}\rvert^2\rangle}}$
Conformity coefficient ([46])	$\mu_{FP} = \frac{2\left(\Re(\langle S_{HH}S^{\star}_{VV}\rangle) - \langle\lvert S_{HV}\rvert^2\rangle\right)}{\langle\lvert S_{HH}\rvert^2\rangle + 2\langle\lvert S_{HV}\rvert^2\rangle + \langle\lvert S_{VV}\rvert^2\rangle}$
Determinant of the sample covariance matrix ([2] [3])	$\det(\boldsymbol{C}_{(FP)})$
Span of the sample covariance matrix ([45])	$\mathrm{span}(\boldsymbol{C}_{(FP)})$
Copolarization difference ([3] [47])	$\mathrm{PD} = \langle\lvert S_{HH}\rvert^2\rangle - \langle\lvert S_{VV}\rvert^2\rangle$
Cross-polarization ratio	$P_X = \frac{\langle\lvert S_{HV}\rvert^2\rangle}{\langle\lvert S_{HH}\rvert^2\rangle + \langle\lvert S_{VV}\rvert^2\rangle}$
Eigenvalues of the sample covariance matrix	$\lambda_1 > \lambda_2 > \lambda_3$
Entropy ([9] [46] [45] [48] [49] [50] [51])	$H = -\sum_{i=1}^{3} p_i \log_3 p_i, \quad p_i = \frac{\lambda_i}{\sum_{i=1}^{3}\lambda_i}$
Mean α angle of eigenvectors	$\langle\alpha\rangle = \sum_{i=1}^{3} p_i \cos^{-1}(\boldsymbol{e}_i(1))$
Anisotropy	$A = \frac{\lambda_2 - \lambda_3}{\lambda_2 + \lambda_3}$
Polarization fraction	$PF = 1 - \frac{\lambda_3}{\lambda_1 + \lambda_2 + \lambda_3}$
Pedestal height	$PH = \frac{\lambda_3}{\lambda_1}$

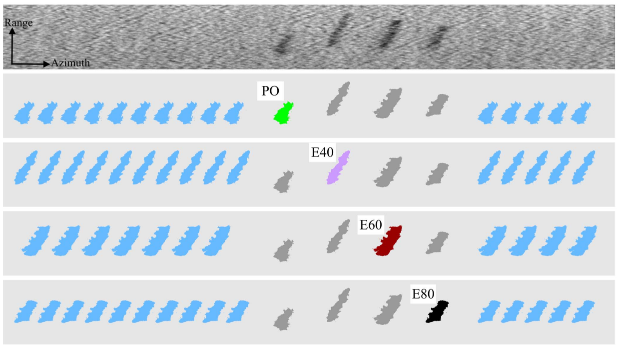

Fig. 5. Top-most figure is the VV-damping ratio of the UAVSAR acquisition taken at 06:26 UTC. The figures below show the segmentation results for each of the four slicks, and the manually selected open water regions to which they are compared. Multiple water regions are used to determine the variance in the clean water properties. The green color represents the PO, and the pink, red, and black colors represent E40, E60, and E80, respectively. Blue color represents open water regions.

V. POLARIMETRIC FEATURES FOR SLICK OBSERVATION

There exists several studies of the performance of oil slick characterization based upon various polarimetric features extracted from the FP and linear–linear DP SAR data evaluated for different ocean and wind conditions, various oil types, and different sensors with various incidence angles and frequencies (see, e.g., [1], [3], [32]). The sensitivity of polarimetric features to the different factors varies. This section presents the most frequently evaluated polarimetric features extracted from the FP and HP SAR data based on previous studies. A rigorous analysis is presented, connecting the Bragg scattering theory discussed in Section II and the polarimetric features here investigated (from both the FP and simulated HP modes).

A. Full-Polarimetric Features

The FP features used in this analysis are given in Table III and their corresponding relation to the components of the Bragg scattering theory is shown in Table IV. Table IV shows all the polarimetric features investigated (both FP and HP) and their dependence on factors in the Bragg scattering theory discussed in Section II. The FP features have all been extensively tested for oil spill characterization and detection, and some corresponding references for these studies are given in parentheses in Table III. In this paper, we observe oil slicks with different chemical and physical properties under high wind conditions and with relatively small volumes of slick material. Hence, some of the FP features reported as having the best performance in the literature may not fulfill their

TABLE IV

POLARIMETRIC FEATURES RELATED TO FACTORS IN THE TWO-SCALE BRAGG SCATTERING THEORY DISCUSSED IN SECTION II. THIS SETUP IS BASED ON THE DISCUSSION OF POLARIMETRIC FEATURES IN SECTION V. NOTE THE INCIDENCE ANGLE IS EITHER θ AND/OR THE LOCAL θ_i (SEE SECTION II)

Factors	Polarimetric features	
- Large-scale roughness - Small-scale roughness - Incidence angle - Dielectric properties	FP	ζ_{HH}, ζ_{VV}, ζ_{HV}, r_{CO}, i_{CO}, det($\boldsymbol{C}_{(FP)}$), span($\boldsymbol{C}_{(FP)}$), PD, λ_1, λ_2, λ_3
	HP	ζ_{RH}, ζ_{RV}, ζ_{RR}, ζ_{RL}, q_0, q_1, q_2, q_3, λ_1^{HP}, λ_2^{HP}, det($\boldsymbol{C}_{(RH,RV)}$), det($\boldsymbol{C}_{(RR,RL)}$)
- Large-scale roughness - Incidence angle - Dielectric properties	FP	γ_{CO}, ρ_{CO}, μ_{FP}, P_X, ϕ_{CO}, H, $\langle\alpha\rangle$, A, PF, PH
	HP	DoP, χ, δ, α, μ_E, $\gamma_{RV/RH}$, $\rho_{(RH,RV)}$, $\phi_{(RR,RL)}$, $\rho_{(RR,RL)}$, $\phi_{(RH,RV)}$, H_w, μ_{HP}

potential in our case, as already highlighted in [19]. Using one of the UAVSAR acquisitions, Skrunes *et al.* [19] showed that the best features for separating the various oil slicks from the open water region were the VV-intensity, the geometric intensity, the largest eigenvalue of the polarimetric decomposition, the real part of the copolarization cross product, and the span (as defined in Table III). These features had the highest separability (the Fisher discriminant ratio) between the four slicks and the open water.

The damping ratios have been shown to be good features for evaluating the contrast between the slick-free and slick covered surfaces in SAR imagery (see, e.g., [1], [3], [41], [42]). Both measured and simulated damping ratios are reported to decrease with increasing wind speed and to increase with frequency (Bragg wavenumber), oil viscosity, and thickness [41], [42]. The damping ratio is a function of the Bragg coefficients and the 2-D wavenumber spectral density of the ocean surface roughness [1]. The change in the effective dielectric constant decreases the backscatter power only if the oil spill is sufficiently thick or if the oil slick is mixed into the water in high enough concentration in a layer below the surface [13]. The oil slicks in our case are quite small in volume and areal extent. Skrunes *et al.* [19] estimated the thickness of the emulsion slicks to be in the range of 1.3–1.7 and 0.7 μm for the PO in the UAVSAR scene acquired at 06:26 UTC. The expected penetration depth for the L-band radar is much higher than these thicknesses. The radiation penetrates to the underlying seawater surface from which it scatters, and the ratio between the Bragg coefficients between the open water and the oil slick is approximately unity, because the scattering occurs mainly from the water interface [1]. The damping ratios are located in the first frame in Table IV. Damping ratios extracted from L-band UAVSAR imagery covering the Deepwater Horizon oil spill were discussed in [1]. It was shown that the HH was dampened slightly less than the VV and HV.

The copolarization power ratio is the ratio between the intensity of the complex scattering coefficients in the HH and VV channels. This feature has been found useful in several studies [1], [2]. In the tilted Bragg model, the copolarization power ratio is independent of the damping of gravity-capillary waves by the oil and is sensitive to the dielectric constant, the large-scale roughness, and the incidence angle [1]. Based on this, the copolarization power ratio is placed in the last frame in Table IV. In general, the ocean wave spectrum is independent of the polarizations. Following this, all the polarimetric features that are composed of ratios are independent of the ocean wave spectrum and depend only on the angles related to the slope and tilt, the incidence angle, and the dielectric properties.

The real part of the copolarization cross product has been shown to be a useful feature for detecting oil. Skrunes *et al.* [2] observed a decrease in correlation when moving from slick-free to slick-covered areas when using spaceborne SAR data. A difference in correlation was also observed using one of the UAVSAR scenes from the NORSE2015 experiment [19]. The physical mechanism behind the change in the correlation of the copolarization channels is yet unknown, but Bragg versus non-Bragg scattering, lower backscatter response for slick-covered surface, and change in scattering mechanism are some theories related to this feature. In the tilted Bragg model, no terms cancel out for this feature, and hence, this feature is in the top row of Table IV, depending on all the factors in the tilted Bragg model.

Another feature frequently used for slick detection is the standard deviation of the phase difference between the copolarization scattering coefficients. This feature is related to the target's properties and measures the degree of correlation between S_{HH} and S_{VV} [52]. Migliaccio *et al.* [4] used this feature to characterize the scattering return from oil spills and biogenic slicks. They differentiated the mineral oil from the clean sea under low-to-moderate wind conditions, and found higher values of the standard deviation of the phase difference for the mineral oil. Migliaccio *et al.* [4] and Schuler *et al.* [43] observed that the low values of this feature represented the presence of Bragg scattering and that an increase in this feature indicated departure from the Bragg regime. However, there is a lack of research on how this feature behaves when using high SNR SAR data. As discovered in [1] and [19], Bragg scattering was observed for the oil slick regions as well as in the open water areas. Therefore, using this feature to separate the oil from open water could be a challenging task, as a similar scattering mechanism might be present in both the regions. The phase difference is located in the bottom panel in Table IV, and this is because this feature contains a ratio between the imaginary and real part of the copolarization correlation coefficients (see, e.g., [53]), making it independent of the ocean wave spectrum.

The magnitude of the copolarization correlation coefficient ($\rho_{(\mathrm{CO})}$) is a multipolarization feature with values between 0 and 1. The low values of $\rho_{(\mathrm{CO})}$ indicate depolarization effects. These effects are sensitive to the presence of a complex surface, multiple scattering surface layers, and/or system noise [53]. This feature will be a function of the root mean square slope (large-scale roughness), the dielectric constant, and the incidence angle [2] (as shown in Table IV).

Studies related to this feature have found low values (low HH–VV correlation) for oil covered areas, and high values for open water regions using both the C- and X-band SARs [2], [44].

Another polarimetric feature that uses multipolarization data is the determinant of the sample covariance matrix. This feature is also similar to the geometric intensity (defined in [2]). Skrunes *et al.* [2] discovered that the geometric intensity gives good contrast between oil slicks and sea for both the X- and C-band SAR data with relatively high incidence angles. They also discovered lower values of this feature for slick-covered areas compared with slick-free areas. Neither the span nor the determinant of the sample covariance matrix contains the ratios of scattering coefficients, and hence, these features are given in the top row in Table IV.

Features related to the eigenvalues and the eigenvectors of the FP sample covariance matrix are also considered. The ones evaluated in this paper, for the FP case, are the eigenvalues, entropy (H), anisotropy (A), polarization fraction (PF), and mean alpha angle ($\langle\alpha\rangle$). The entropy contains information regarding the degree of randomness of the scattering process, while the anisotropy represents the relative importance of the second and third eigenvalues [54]. These features are all composed of ratios of eigenvalues extracted from the covariance matrix, and we can therefore assume, following the two-scale Bragg model, that these features are independent on the small-scale roughness and are only a function of the large-scale roughness, dielectric properties, and incidence angle (as reflected in the second frame in Table IV).

B. Hybrid-Polarity Features

The polarimetric features extracted from the simulated HP data used in this analysis are given in Table V, with the corresponding references given in parentheses. The Stokes vector is a popular feature when analyzing HP data. The expression for the Stokes vector for linear receive polarization is given in Table V. Each of the Stokes parameters is tested in this paper, where the first Stokes parameter (q_0) is the total power, the second, q_1, is the power in the linear horizontal or vertical polarization, q_2 is the power in the linearly polarized components at tilt angles 45° and 135°, and q_3 is equal to the power in the left-handed and right-handed circular polarizations [54]. Brekke *et al.* [18] showed that the imaginary part of the RH and RV (q_3) follows the same trend as the copolarization cross product, which has lower correlation for the oil slicks than for clean water. Following the two-scale Bragg model of the HP data, q_0 and q_3 are a function of the tilt angles, wave spectrum, incidence angle, and the dielectric properties, while q_1 and q_2 depend on the same terms, in addition to the rotation angle (as shown in Section II-B).

Child parameters of the Stokes vector evaluated in this paper are the degree of polarization (DoP), the ellipticity angle (χ), the circular-polarization ratio (μ_E), the relative phase (δ), and the alpha angle (α). The DoP has been extensively used in the literature [10], [12], [56], and describes the degree of depolarization in the measured signal backscattered from a given surface element. The DoP has been extensively used in the literature (see, e.g., [10], [12], [56]). The χ feature is used in the $m - \chi$ (where m is DoP) decomposition [58], and this feature could help in distinguishing the even versus odd bounce scattering. If the open water and the oil slicks posses different scattering mechanisms, the resulting separability would be high for this feature. The features χ, μ_E, δ, and α are ratios of the Stokes parameters. In the two-scale Bragg model (see Section II), these features are independent of the ocean wave spectrum (the damping of the gravity-capillary waves by oil). This indicates that these features are the function of the dielectric constant, the incidence angle, and the large-scale roughness (see second frame in Table IV).

The hybrid-polarization power ratio is the ratio between the intensity of the simulated complex scattering coefficients in the RH and RV channels. Since the copolarization intensities have higher response than the cross-polarization intensity, the hybrid-polarization ratio is expected to have approximately the same behavior as the copolarization ratio discussed in Section V-A. Hence, this feature is also independent of the ocean wave spectrum. The standard deviation of the phase difference between the RH and RV scattering coefficients has been found to be a good feature for oil spill detection [10]. We also test the standard deviation of the phase difference between the RR and RL scattering coefficients.

The magnitude of the hybrid-polarization correlation coefficients are also considered, both in circular–linear and circular–circular basis, i.e., $\rho_{(\mathrm{RH,RV})}$ and $\rho_{(\mathrm{RR,RL})}$. $\rho_{(\mathrm{RR,RL})}$ was introduced in [10], and they named it the HP coherence measure. The authors in the same article demonstrated this feature on five Radarsat-2 scenes covering various types of oil. From the figures in [10], one can see that the low values of $\rho_{(\mathrm{RR,RL})}$ are present for the oil slick regions and high values for the open water areas, which is the same behavior as $\rho_{(\mathrm{CO})}$. We concluded that this feature could suppress some lookalikes caused by low wind and also generated good slick-sea contrast. Zhang *et al.* [9] also found the low values of $\rho_{(\mathrm{RH,RV})}$ for oil covered areas and high values for open water using both the L- and C-band SARs. These features are located in the last row of Table IV, where $\rho_{(\mathrm{RH,RV})}$ and $\rho_{(\mathrm{RR,RL})}$ are independent of the small-scale roughness, since these features are composed of ratios.

The conformity coefficient is a multipolarization feature containing both cross- and co-polarization intensities and correlation. The FP variant of this feature can be seen in Table III, and to calculate this feature, the reflection symmetry assumption must be made. Zhang *et al.* [46] stated that this feature can be used to distinguish different scattering mechanisms of ambient sea surfaces and slicks. They concluded that when μ was positive, Bragg scattering took place, and the pixels producing such values were classified as slick free area. Negative values was defined as non-Bragg scattering and thus classified as slick-covered areas. However, Minchew *et al.* [1] discovered that Bragg scattering was present within the slick-covered areas, and this feature might therefore not follow the theory suggested in [46] for separating the oil slicks from open water using the UAVSAR data. The conformity coefficients, $\rho_{(\mathrm{RH,RV})}$ and $\rho_{(\mathrm{RR,RL})}$, contain the ratios of scattering coefficients, and since the ocean wave spectrum is polarization

TABLE V

OVERVIEW OF THE INVESTIGATED HP (WITH RIGHT CIRCULAR TRANSMITS AND LINEAR RECEIVE) FEATURES (COMPUTED USING A MASK OF 15 × 60 PIXELS). THE REFERENCES INCLUDED ARE THE EXAMPLES OF STUDIES WHERE THE FEATURES HAVE BEEN INVESTIGATED FOR OIL SPILL OBSERVATION. THE "CIRCULAR-LINEAR" BASIS DENOTES THE HP FEATURES, WHILE THE "CIRCULAR–CIRCULAR" DENOTES THE HP FEATURES PROJECTED INTO THE CIRCULAR TRANSMIT AND CIRCULAR RECEIVE BASIS

HP Features (based on measuring RH and RV)	
Name	Formula
Stokes vector ([6] [56])	$\boldsymbol{q} = \begin{bmatrix} q_0 \\ q_1 \\ q_2 \\ q_3 \end{bmatrix} = \begin{bmatrix} \langle \lvert S_{RH}\rvert^2 + \lvert S_{RV}\rvert^2 \rangle \\ \langle \lvert S_{RH}\rvert^2 - \lvert S_{RV}\rvert^2 \rangle \\ 2\Re\langle (S_{RH}S_{RV}^{\star})\rangle \\ -2\Im\langle (S_{RH}S_{RV}^{\star})\rangle \end{bmatrix} = \begin{bmatrix} \langle \lvert S_{RR}\rvert^2 + \lvert S_{RL}\rvert^2 \rangle \\ 2\Re\langle (S_{RR}S_{RL}^{\star})\rangle \\ 2\Im\langle (S_{RR}S_{RL}^{\star})\rangle \\ -\langle \lvert S_{RL}\rvert^2 - \lvert S_{RR}\rvert^2 \rangle \end{bmatrix}$ (circular-linear) (circular-circular)
Degree of polarization ([10] [12] [57])	$\mathrm{DoP} = \frac{\sqrt{q_1^2+q_2^2+q_3^2}}{q_0}$
Ellipticity angle ([10] [57])	$\chi = \frac{1}{2}\sin^{-1}(-\frac{q_3}{DoP\ q_0})$
Relative phase ([7]) and alpha angle ([58])	$\delta = \frac{1}{2}\tan^{-1}(\frac{q_3}{q_2}) \quad \alpha = \frac{1}{2}\tan^{-1}(\frac{q_1+q_2}{q_3})$
Damping ratio	$\zeta_{ij} = 10\ \log_{10}\left(\frac{\langle I_{ij}^{(sea)}\rangle}{\langle I_{ij}^{(slick)}\rangle}\right)$, where $I_{ij} = \lvert S_{ij}\rvert^2$ $(i,j) \in$ ((R,H) $\vee$ (R,V)) $\vee$ ((R,R) $\vee$ (R,L)) (circular-linear) (circular-circular)
Circular-polarization ratio ([9])	$\mu_E = \frac{q_0-q_3}{q_0+q_3}$ $\Big($also equal to: $\gamma_{RR/RL} = \frac{\langle I_{RR}\rangle}{\langle I_{RL}\rangle}\Big)$
Hybrid-polarization power ratio ([35])	$\gamma_{RV/RH} = \frac{\langle I_{RV}\rangle}{\langle I_{RH}\rangle}$
Correlation coefficient ([10] [9])	$\rho_{(RH,RV)} = \frac{\lvert(S_{RH}S_{RV}^{\star})\rvert}{\sqrt{\langle\lvert S_{RH}\rvert^2\rangle\langle\lvert S_{RV}\rvert^2\rangle}}$ (circular-linear) $\rho_{(RR,RL)} = \frac{\lvert(S_{RR}S_{RL}^{\star})\rvert}{\sqrt{\langle\lvert S_{RR}\rvert^2\rangle\langle\lvert S_{RL}\rvert^2\rangle}}$ (circular-circular)
Standard deviation of the phase difference	$\phi_{(RH,RV)} = \sqrt{\langle(\phi_{RH}-\phi_{RV})^2\rangle + (\langle\phi_{RH}-\phi_{RV}\rangle)^2}$ (circular-linear) $\phi_{(RR,RL)} = \sqrt{\langle(\phi_{RR}-\phi_{RL})^2\rangle + (\langle\phi_{RR}-\phi_{RL}\rangle)^2}$ (circular-circular)
Eigenvalues	$\lambda_{1,2}^{HP} = q_0 \pm \sqrt{q_1^2+q_2^2+q_3^2}$
Entropy (wave entropy) ([9])	$H_w = -\sum_{i=1}^{2} p_i \log_2 p_i, \qquad p_i = \frac{\lambda_i^{HP}}{\sum_{i=1}^{2}\lambda_i^{HP}}$
Conformity coefficient ([10] [46])	$\mu_{HP} = \frac{2\Im\langle S_{RH}S_{RV}^{\star}\rangle}{\langle\lvert S_{RH}\rvert^2\rangle+\langle\lvert S_{RV}\rvert^2\rangle}$
Determinant of the covariance matrix	$\det(\boldsymbol{C}_{(RH,RV)}) = \det\left(\begin{bmatrix} \langle\lvert S_{RH}\rvert^2\rangle & \langle S_{RH}S_{RV}^{\star}\rangle \\ \langle S_{RV}S_{RH}^{\star}\rangle & \langle\lvert S_{RV}\rvert^2\rangle \end{bmatrix}\right)$ (circular-linear) $\det(\boldsymbol{C}_{(RR,RL)}) = \det\left(\begin{bmatrix} \langle\lvert S_{RR}\rvert^2\rangle & \langle S_{RR}S_{RL}^{\star}\rangle \\ \langle S_{RL}S_{RR}^{\star}\rangle & \langle\lvert S_{RL}\rvert^2\rangle \end{bmatrix}\right)$ (circular-circular)

independent, these features become independent of the ocean wave spectrum, as given in the second frame in Table IV.

The determinant of the simulated sample HP covariance matrix, both in the circular–linear and circular–circular basis, is also evaluated. We did not find studies related to these two features in the HP scenario. Unfortunately, the HP sample covariance matrix is 2-D, and the anisotropy is not available, since it requires the two minimum eigenvalues from a 3-D matrix. This is only possible if a reconstruction of a pseudo-FP covariance matrix is performed. The HP entropy (known as the wave entropy), however, can be calculated from the Stokes vector. This was done for an oil spill study in [9], and was found to have the same behavior as the FP entropy, that is, large for slick-covered areas and low for slick-free areas.

VI. RESULTS AND DISCUSSION

In Sections VI-A–VI-D, the results obtained from the analysis of the UAVSAR time series are presented. The simulated HP features are compared with the FP features in terms of slick detectability. The change in separability based upon the best FP and HP features as a slick evolves naturally on the sea surface is also discussed. The results obtained from the simulated HP features are also compared with the previous findings.

A. Noise Analysis

As is already known, the returns from the oil slicks are low, and hence, a noise analysis of the data used is important. The minimum backscattered signal that can be detected from a given surface element is dependent on the system's *noise floor*. The noise floor, related to the *noise equivalent sigma zero* (NESZ), is extremely low for the UAVSAR instrument (NESZ in the range of −48 to −33 dB [5]) compared with other sensors such as Radarsat-2 (NESZ in the range of −27.5 to −43 dB [59]) and TerraSAR-X (NESZ in the range of −19 to −26 dB [60]). Several studies of the effect

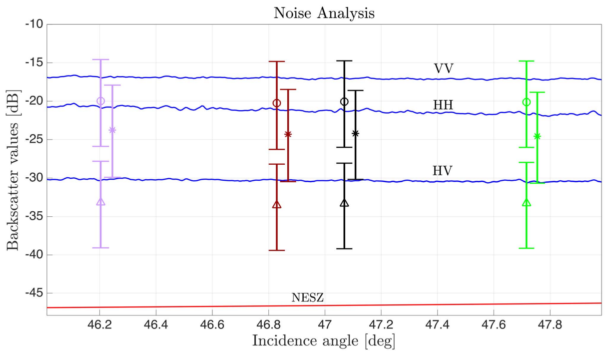

Fig. 6. Noise analysis from the UAVSAR scene taken at 06:26 UTC (ascending). The 5th, 50th, and 95th percentiles are calculated for each slick region, and plotted with a vertical line from the 5th to the 95th percentile, and a symbol indicating the 50th percentile: a circle for VV, a star for HH, and a triangle for HV. The lines for HH are slightly shifted to higher incidence angle to improve the discrimination in the plot. The blue continuous lines show the 50th percentile for clean sea samples selected along the range direction.

of the NESZ on radar-dark surfaces, such as oil slicks, have been conducted using spaceborne SAR sensors [2], [3], [61], and have shown that a large part of the cross-polarization return and also some part of the copolarization return from oil slicks are near or even below the instrument noise floor. RISAT-1 is the first spaceborne satellite that offers the circular or HP imaging mode. Unfortunately, the NESZ is high, -17 dB, for the RISAT-1 FRS-1 mode [62]. A consequence of returns below the NESZ is loss of information, and even though the slick can be detected through comparison with clean water signals above the NESZ, oil spill characterization may not be possible.

The NESZ for the UAVSAR varies between -48 dB at the point of maximal antenna gain and -33 dB in the far range [5]. Such a low NESZ is important for our application as our goal is analyzing the backscattered response from the various slicks, in addition to simulating the HP data from the FP data, resulting in a mix of co- and cross-polarization channels and a 3-dB power loss when simulating the HP scattering vector [8]. The HP intensities are still above the noise floor for all the UAVSAR scenes used in this analysis. We demonstrate this using one scene in Fig. 6, and the other scenes show a similar trend.

Fig. 6 shows an example of the noise analysis we performed. The 5th, 50th, and 95th percentiles of the HH, VV, and HV intensities are calculated for each region. No multilooking and incidence angle correction has been done prior to the noise analysis in order to show the characteristics of the different intensities of the actual measured values at the highest instrument resolution. The 50th percentiles are indicated by various symbols depending on the polarization used. The blue continuous lines show the 50th percentile for clean sea samples selected along the range direction for the three intensities. Following [1], an acceptable return was suggested to be 6 dB above the noise floor, i.e., 20% of the measured signal is noise, and 80% is the signal backscattered. The NESZ is indicated by the red continuous line in Fig. 6. The NESZ as a function of incidence angle is found in [5]. The HH intensities are slightly below the VV intensities but well above the NESZ + 6 dB limit. This is also the case for the other UAVSAR scenes used in this analysis. Hence, the noise should not have a significant impact on the various polarimetric features extracted from the UAVSAR scenes. Similar results are found in [19] for one UAVSAR acquisition from the NORSE2015 experiment.

B. Slick Separability Based on FP and HP Features

The polarimetric feature values are calculated for each region (different slicks and open water), and their statistical properties used as an input in the calculation of the JM separability measure. Figs. 7–10 show the charts of the mean JM separability for all of the polarimetric features for slick versus open water. The separability between the various slicks is not shown, because the JM separability is below 0.6 for all cases. Note that the JM separability is calculated between each slick and its corresponding subset of open water regions (as shown in Fig. 5). This result in several JM distances, and the average of these are shown in the color charts in Figs. 7–10. Due to space limitation, the standard deviation of the JM measures is left out, but these are shown later for the features with the maximum JM separability. Note that the features in the color charts are sorted so that the JM separability decreases from the top of the chart to the bottom. In Figs. 7–10, the red color indicates the highest separability between the slick and the open water. Red, orange, yellow, green, dark, and light blue colors indicate separability, in decreasing order. Using color charts, we obtain a good overview of all the polarimetric features, and can more easily identify the best ones.

The FP color chart in Fig. 7, representing the average separability between PO and the OW regions, is the one that contains highest separability for the various features along the time series compared with the other emulsion slicks and open water (both for FP and HP). The FP features that provide high separability between the PO and open water are ζ_X (damping ratio) with seven red and ten orange cells along the time series, and second is the λ_3 (minimum eigenvalue) with nine red and seven orange cells. In other words, using the ζ_X feature, the PO can be differentiated from open water in 17 out of 18 scenes with relatively high separability.

These two features are also among the best at providing high separability for the emulsion slicks. Considering the FP separability color charts for E40, both the ζ_X and λ_3 features give high separability for three scenes in the times series. For the two first scenes, several FP features can be used to distinguish either E40 or E60 from the open water regions. The E40 has high separability ($\mathrm{JM} > 0.8$) in 8 out of 18 scenes using various features, while the E60 has high separability in 9 out of 18 scenes. The ζ_{VV} and the PF features provide higher detectability of E60 than E40. The FP color chart representing the separability between E80 and OW is shown in Fig. 10. Here, the first acquisition at 05:32 UTC is not included, because this oil had not been released. This color chart contains several orange cells, more than the E40 and E60 FP color charts, which indicates higher overall detectability of E80 than E60 and E40. Again, ζ_X and λ_3 stand out, followed

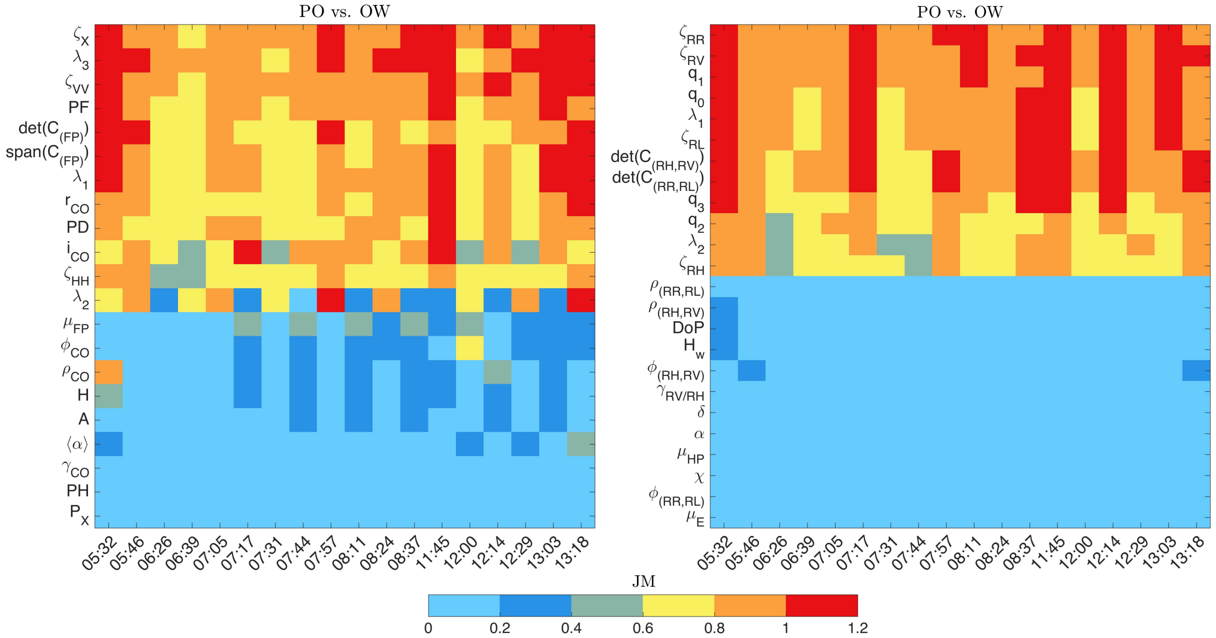

Fig. 7. Color charts of the JM separability between PO and OW for the FP (left chart) and the HP (right chart) features. Red, orange, yellow, green, dark, and light blue indicate separability, in decreasing order. The x-axis represents the acquisition time (in UTC).

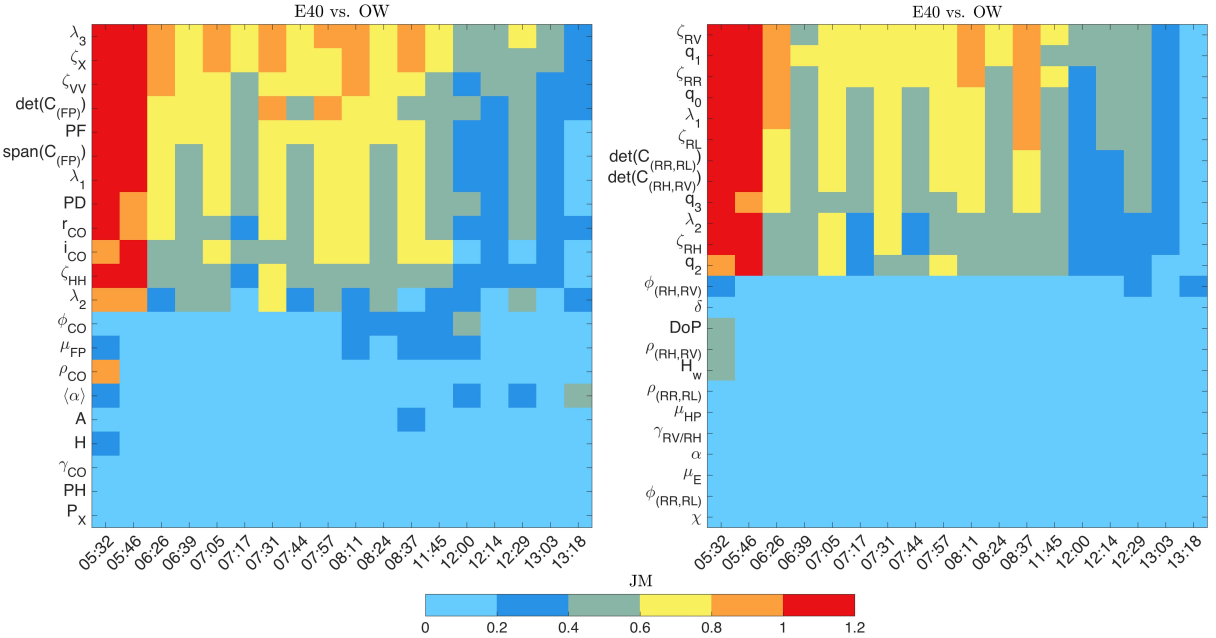

Fig. 8. Color charts of the JM separability between E40 and OW for the FP (left chart) and the HP (right chart) features. Red, orange, yellow, green, dark, and light blue indicate separability, in decreasing order. The x-axis represents the acquisition time (in UTC).

by det($\mathbf{C}_{(\mathrm{FP})}$), PF, and PD. A more in-depth analysis of how the JM changes with time for the various oil slicks is given in Section VI-C. The FP features that are not able to separate the various slicks from open water are γ_{CO}, P_X, ϕ_{CO}, ρ_{CO}, PH, μ_{FP}, H, $\langle\alpha\rangle$, and A, according to the threshold that is set for the JM distance. One previous study related to the use of UAVSAR L-band for oil spill observation (Deepwater Horizon oil spill) was presented in [1]. Minchew *et al.* [1] discovered that $\langle\alpha\rangle$ was sensitive to the change in the dielectric constant rather than damping of the ocean waves. To detect the oil using $\langle\alpha\rangle$,

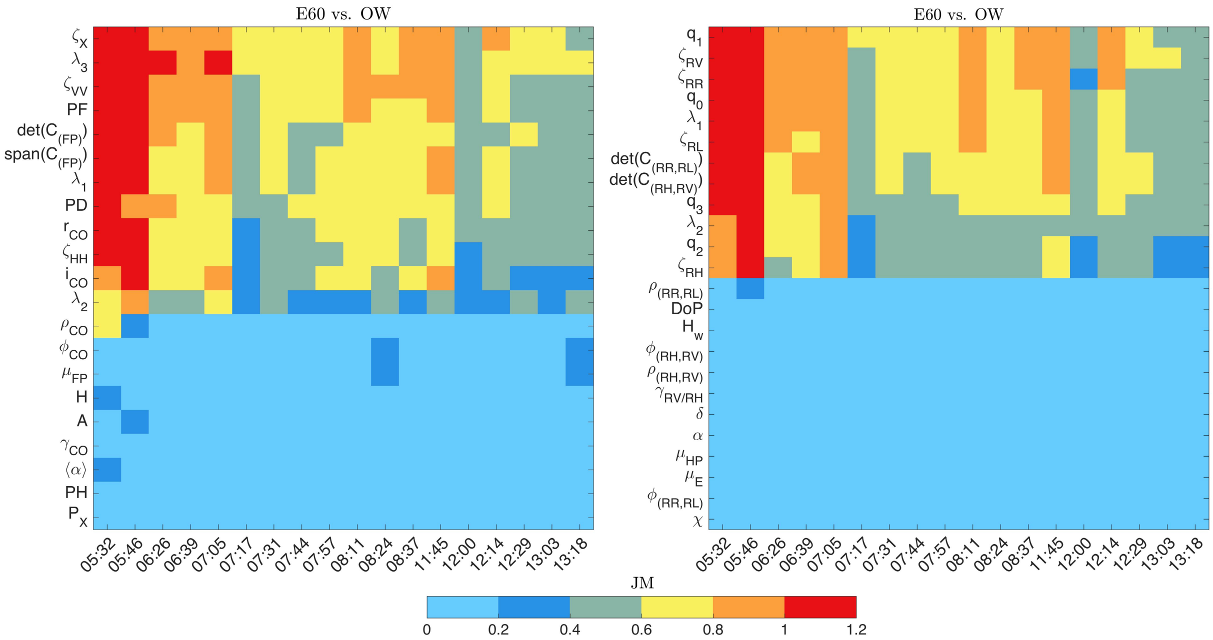

Fig. 9. Color charts of the JM separability between E60 and OW for the FP (left chart) and the HP (right chart) features. Red, orange, yellow, green, dark, and light blue indicate separability, in decreasing order. The x-axis represents the acquisition time (in UTC).

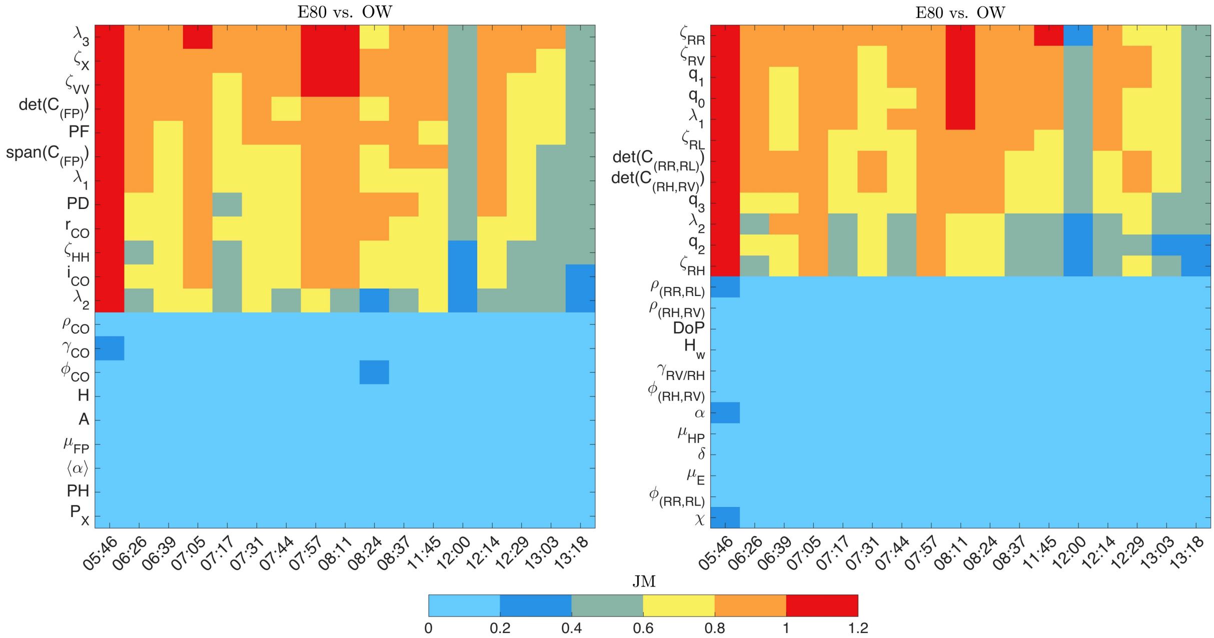

Fig. 10. Color charts of the JM separability between E80 and OW for the FP (left chart) and the HP (right chart) features. Red, orange, yellow, green, dark, and light blue indicate separability, in decreasing order. The x-axis represents the acquisition time (in UTC).

it is required that the oil must mix with the ocean to create an intermediate dielectric layer and/or the oil slick is sufficient thick enough (see Section I). The low separability values of $\langle\alpha\rangle$ in our case might indicate that such a layer was not presented. Minchew *et al.* [1] also discovered, based on the entropy (H), that both the oil slicks and open water had one dominant scattering mechanism, namely, the Bragg scattering. Therefore, it is challenging to use the entropy to separate the oil slicks from the clean sea, as the same scattering characteristics might be present. Although it has been suggested that the entropy is sensitive to slick-covered surfaces (high entropy for slick-covered surface and low entropy for slick-free surface) in several studies using spaceborne SAR data under various wind conditions [32], [45], [48], [51], this is not the case for our data set. The set of features that are incapable of separating the four oil slicks from the open water region are all located in the bottom panel in Table IV. The top best features for detecting the various oil slicks are located in the top panel in Table IV. This indicates that the features independent on the small-scale roughness show poor detection capabilities, while features containing the small-scale roughness show good detectability.

Previous studies have found that det($\boldsymbol{C}_{(\mathrm{FP})}$) (only using co-polarization products) and r_{CO} are best at distinguishing biogenic slicks from mineral oil under low wind conditions, in this case using Radarsat-2 C-band data [2]. det($\boldsymbol{C}_{(\mathrm{FP})}$) and r_{CO} in our case have JM above 0.5 in all scenes, but they do not separate as well as the ζ_X and λ_3 features. The same study [2] did exclude features that contained the cross-polarization scattering coefficients, because they had a large part of the signal below the noise floor. Using the UAVSAR data, the noise is no longer an issue for the cross-polarization scattering components, and we are now able to see the usefulness of the cross-polarization feature, for example, the high separability of the ζ_X and λ_3 features. The reasons why the cross-polarization feature is the best for detecting the oil should be further investigated. One theory could be that the cross-polarization intensity is closer to the noise floor compared with the copolarization intensities. Other theories could be related to the depolarization effects caused by the dielectric properties within the oil or that the tilt angles are larger for high wind conditions. The good potential of the cross-polarization feature was also highlighted using UAVSAR data from the Deepwater Horizon oil spill [1], and also in one of the UAVSAR scenes from the NORSE2015 experiment [63].

The right panels in Figs. 7–10 show the color charts for the HP features along the time series. Fewer red colored cells are observed for the PO versus OW HP color chart compared with the PO versus OW FP color chart. Unfortunately, the polarimetric features containing the cross-polarization component are no longer possible to separate out in the HP mode. The HP features that have high separability between PO and OW, in decreasing order, are ζ_{RR}, ζ_{RV}, q_1, q_0, λ_1, ζ_{RL}, det($\boldsymbol{C}_{(\mathrm{RH,RV})}$), det($\boldsymbol{C}_{(\mathrm{RR,RL})}$), and q_3, respectively. The same features also provide high separability for the emulsion slicks. The HP features that are comparable with the FP features show similar colors of the JM separability, for example, ζ_{RV} and ζ_{RH} show similar separability values as ζ_{VV} and ζ_{HH} for all the various slicks. $\gamma_{\mathrm{RV/RH}}$, $\phi_{(\mathrm{RH,RV})}$, $\phi_{(\mathrm{RR,RL})}$, $\rho_{(\mathrm{RR,RL})}$, $\rho_{(\mathrm{RH,RV})}$, μ_{HP}, H_w, DoP, χ, and μ_E are features that achieve low separability between the various slicks and open water for all the UAVSAR scenes. This corresponds well with the setup in Table IV, where the features resulting in high separability are dependent on, amongst other, the small-scale roughness, and the features showing low separability are independent of this factor. This was also found for the corresponding FP features, namely, γ_{CO}, ϕ_{CO}, μ_{FP}, and H. Hence, we are left with 12 HP features that perform reasonably well at separating the various oil types from the open water regions. For the emulsions slicks, the E40 versus OW HP color chart has the minimum number of orange colored cells, followed by E60 versus OW and E80 versus OW HP color charts. This is the same behavior as the FP color charts for the emulsion slicks.

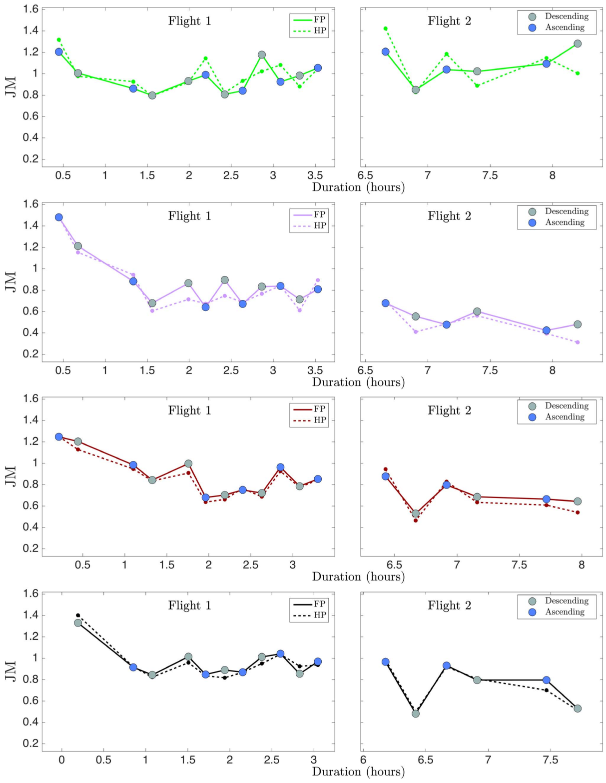

Fig. 11. Maximum JM distance obtained from all the polarimetric features along the time series. The points represent the maximum mean JM distance, and the solid (dashed) lines represent the values between these for the FP (HP) features. The green, pink, red, and black colors represent the JM separability between the PO versus OW, E40 versus OW, E60 versus OW, and E80 versus OW. The blue and gray markers represent the ascending and descending scenes.

Previous studies related to the HP features simulated from spaceborne FP SAR have obtained different results. Salberg *et al.* [10] used the same data set as [2], and discovered that $\rho_{(\mathrm{RR,RL})}$ (Salberg *et al.* [10] named this feature Coh), the conformity index μ_{HP}, and the DoP can be used to detect various types of oil (plant, emulsion, and crude oil), using C-band data under low-to-moderate wind condition. Nunziata *et al.* [9] concluded based on L- and C-band spaceborne SAR data that the wave entropy (H_w), circular-polarization ratio (μ_E), $\rho_{(\mathrm{RR,RL})}$, and the relative intensity of the polarized component to the intensity of the total field could discriminate slick-free, weak-damping slick covered, and strong-damping slick-covered sea surfaces. Additionally, [64] also concluded that the DoP could be used to detect the oil spills from the ocean surface using both C-band SAR and L-band UAVSAR data. The separability observed in our color charts do not agree with the findings in [9], [10], and [65], which may be due to several factors, including the high wind, the small slicks, and the fact that the data used in this paper are well above the noise floor.

The highest JM separabilities obtained from both the FP and HP features across the entire UAVSAR time series are shown in Fig. 11. The green, pink, red, and black colors represent the highest mean JM separability for the PO versus OW, E40 versus OW, E60 versus OW, and E80 versus OW, respectively. The FP and HP features that provide the highest mean JM and the corresponding standard deviation of the JM between the slick and the open water regions (see Fig. 5) are given in Table VI. Note that the feature for which the JM separability is highest can change as the slick evolves. For comparison, the highest JM separability obtained using the HP features is plotted as a dashed line in the same figure as the highest JM separability using the FP features. The x-axis represents the time since release of each slick, not the time since the first image was acquired. Because the slicks were not all released simultaneously, the x-axis is shifted for each of the slicks. The UAVSAR time series was collected in two flights, and hence, each panel in Fig. 11 is divided into two subplots. Additionally, the difference between the ascending and the descending scenes are marked with green and gray colored dots.

There are two ways to evaluate the information in Table VI and Fig. 11. The first is to study how the separability between the various slicks and the open water regions varies with time and how the weathering process of the emulsion and PO slicks affects the detectability. The second way is to identify the polarimetric features that give the highest JM separability as a function of time for the various slicks. Each of these two evaluations will be discussed in Sections VI-C and VI-D.

C. Separability as a Function of Time

The first flight covers approximately the first 4 h after release, while the second flight covers approximately 6.5–8.5 h following release of the oils, with some variation, because the PO was released first and the E80 last. From Fig. 11, we find that the JM separability between the PO and the open water regions starts off at 1.2 and then decreases over the next 2 h. The separability increases again during the next half an hour. During the remaining hours of flight 1, the separability fluctuates, and in the last hour of flight 2, the separability increases again. From the intensity images in Fig. 1, the PO reaches an equilibrium in terms of shape and size in the beginning of flight 2 and remains visible throughout the time series.

The separability of the emulsion oils from the open water regions generally decreases with time with some fluctuations along the way. The separability is higher between the E80 and the open water regions along the time series compared with the other emulsion slicks. This might be a result of the higher oil fraction in E80 compared with E60 and E40. The viscosities of the emulsion slicks are characterized by higher viscosity than the natural film [65]. Hence, the emulsion slicks should have a stronger damping of the ocean waves and thus be more detectable than the PO. Both Figs. 7 and 11 show that this is not the case, and the PO is visible longer on the sea surface than the emulsion slicks. Hence, the PO compound used, Radiogreen EBO, might therefore not be a good indicator for simulating biogenic slicks, as already stated in [20].

It is challenging to segment out the emulsion slicks for the UAVSAR scenes in flight 2, which results in higher presence of the open water in these segments. This might be because of the emulsion slicks have a higher area and higher westerly extent than the PO (see Fig. 1). Immediately after release, the emulsion slicks might undergo emulsification, i.e., take in additional water molecules into the oil–water mix [66]. Hence, more water can be mixed with the E80, and higher volume over time. Parts of the oil spill might also break up into drops of varying sizes that are mixed down into the water column (dispersion), and the oil droplets might also resurface. A parallel study investigated the oil slicks' drift using two different oil drift models [20]. The model results indicated that the PO entrained more quickly and deeper into the water column compared with the emulsion slicks. Additionally, the PO droplets resurfaced to maintain the observable slick. As a result of the entrainment into the water column, the PO was shielded from the wind drag and Stokes drift, which resulted in longer visibility on the sea surface compared with the emulsion slicks. The same study also compared the E80 slick with the model simulations, and the model results showed that the simulated E80 had ~50% or more of the oil on the surface throughout the simulation, and relatively little penetrated deeper than 10 m. Hence, the emulsion slicks are more exposed to wind drag and Stokes drift, which results in more spreading than the PO experienced.

The separability as a function of time can be affected by several factors, which include the imaging geometry (the difference between ascending and descending), changing wind and ocean state over the time series, weathering processes, and the accuracy of the segmentation for all the scenes. The incidence angle of the PO within the scene varies across the times series (see Fig. 2). The incidence angle has a higher variation in flight 2 scenes compared with flight 1 scenes, which might be the reason for the fluctuations in the separability between the descending and ascending scenes in flight 2. In the Appendix, the incidence angle correction applied to the complex scattering vector in the preprocessing of the UAVSAR scenes was discussed. The fact that the incidence angle affects the separability of the PO might be a result of the texture variation with incidence angle (which is not corrected for), and difference in the imaging geometry between ascending and descending. Finding the best incidence angle correction method that can allow comparison across several scenes (especially the ascending and descending in our case) with slightly different incidence angle is a study in itself and should be further investigated.

The PO is released to simulate biogenic slicks, and the biogenic slick forms a monomolecular layer [67]. Previous studies have found that biogenic surface films disappear in high wind condition (typically above 7–10 m/s) due to entrainment into the underlying water by the breaking waves [16], [67]. The reader is referred to [20] for additional information on how the various oil slicks were transported. In addition, a study on how the polarimetric features are affected by the imaging geometry is on-going.

TABLE VI

MEAN AND STANDARD DEVIATION OF THE JM FROM THE BEST FP (TOP) AND THE BEST HP (BOTTOM) FEATURE ALONG THE TIME SERIES FOR THE VARIOUS OIL SLICKS AND THE OPEN WATER REGIONS

Time (UTC)	PO vs. OW	E40 vs. OW	E60 vs. OW	E80 vs. OW
05:32	ζ_{VV} (1.2 ± 0.1) ζ_{RV} (1.32 ± 0.12)	λ_3 (1.48 ± 0.08) ζ_{RV} (1.49 ± 0.1)	λ_3 (1.25 ± 0.07) ζ_{RV} (1.25 ± 0.09)	ζ_{VV} (0.93 ± 0.1) ζ_{RR} (1.15 ± 0.15)
05:46	λ_3 (1.01 ± 0.11) $\det\big(C_{(RH,RV)}\big)$ (0.98 ± 0.1)	λ_3 (1.21 ± 0.07) $\det\big(C_{(RH,RV)}\big)$ (1.15 ± 0.07)	ζ_X (1.2 ± 0.04) ζ_{RR} (1.13 ± 0.07)	$\det(C_{(FP)})$ (1.33 ± 0.07) $\det\big(C_{(RR,RL)}\big)$ (1.4 ± 0.11)
06:26	ζ_{VV} (0.86 ± 0.06) ζ_{RV} (0.93 ± 0.1)	λ_3 (0.88 ± 0.07) q_1 (0.94 ± 0.1)	λ_3 (0.98 ± 0.06) q_1 (0.95 ± 0.07)	λ_3 (0.92 ± 0.07) ζ_{RR} (0.92 ± 0.08)
06:39	λ_3 (0.8 ± 0.1) q_1 (0.79 ± 0.1)	ζ_X (0.68 ± 0.08) q_1 (0.61 ± 0.09)	ζ_{VV} (0.84 ± 0.06) ζ_{RR} (0.83 ± 0.08)	λ_3 (0.84 ± 0.09) $\det\big(C_{(RR,RL)}\big)$ (0.82 ± 0.12)
07:05	$\det(C_{(FP)})$ (0.93 ± 0.12) ζ_{RR} (0.92 ± 0.14)	λ_3 (0.86 ± 0.12) $\det\big(C_{(RH,RV)}\big)$ (0.71 ± 0.12)	λ_3 (1 ± 0.12) $\det\big(C_{(RR,RL)}\big)$ (0.91 ± 0.12)	λ_3 (1.01 ± 0.1) ζ_{RR} (0.96 ± 0.11)
07:17	i_{CO} (0.99 ± 0.08) ζ_{RR} (1.14 ± 0.07)	ζ_X (0.64 ± 0.13) q_1 (0.67 ± 0.09)	λ_3 (0.68 ± 0.13) q_1 (0.64 ± 0.13)	λ_3 (0.85 ± 0.12) q_1 (0.83 ± 0.14)
07:31	ζ_X (0.81 ± 0.06) q_1 (0.82 ± 0.13)	λ_3 (0.89 ± 0.07) $\det\big(C_{(RH,RV)}\big)$ (0.75 ± 0.11)	λ_3 (0.7 ± 0.07) q_1 (0.66 ± 0.08)	ζ_X (0.89 ± 0.04) $\det\big(C_{(RH,RV)}\big)$ (0.82 ± 0.09)
07:44	ζ_X (0.84 ± 0.06) ζ_{RR} (0.93 ± 0.13)	ζ_X (0.67 ± 0.06) q_1 (0.69 ± 0.09)	ζ_X (0.75 ± 0.05) q_1 (0.76 ± 0.1)	ζ_X (0.87 ± 0.05) q_1 (0.87 ± 0.04)
07:57	λ_3 (1.18 ± 0.06) $\det\big(C_{(RR,RL)}\big)$ (1.02 ± 0.1)	λ_3 (0.83 ± 0.06) ζ_{RR} (0.77 ± 0.1)	ζ_{VV} (0.72 ± 0.06) q_1 (0.69 ± 0.08)	λ_3 (1.01 ± 0.05) ζ_{RR} (0.95 ± 0.1)
08:11	ζ_{VV} (0.92 ± 0.1) ζ_{RR} (1.08 ± 0.09)	λ_3 (0.84 ± 0.12) ζ_{RR} (0.84 ± 0.12)	λ_3 (0.96 ± 0.11) q_1 (0.93 ± 0.12)	λ_3 (1.04 ± 0.1) ζ_{RV} (1.04 ± 0.1)
08:24	λ_3 (0.98 ± 0.06) q_1 (0.88 ± 0.09)	λ_3 (0.71 ± 0.06) q_1 (0.61 ± 0.08)	ζ_{VV} (0.79 ± 0.06) q_1 (0.77 ± 0.07)	ζ_{VV} (0.85 ± 0.05) ζ_{RV} (0.92 ± 0.08)
08:37	ζ_X (1.05 ± 0.08) q_0 (1.04 ± 0.15)	λ_3 (0.81 ± 0.09) ζ_{RV} (0.89 ± 0.16)	λ_3 (0.85 ± 0.09) ζ_{RV} (0.84 ± 0.09)	λ_3 (0.97 ± 0.07) q_1 (0.94 ± 0.07)
11:45	ζ_{VV} (1.21 ± 0.08) ζ_{RR} (1.42 ± 0.13)	ζ_X (0.68 ± 0.08) ζ_{RR} (0.7 ± 0.16)	ζ_X (0.88 ± 0.07) ζ_{RR} (0.94 ± 0.12)	λ_3 (0.97 ± 0.08) ζ_{RR} (0.98 ± 0.14)
12:00	ζ_X (0.85 ± 0.06) q_1 (0.83 ± 0.08)	λ_3 (0.55 ± 0.07) q_1 (0.41 ± 0.1)	λ_3 (0.53 ± 0.06) ζ_{RV} (0.46 ± 0.11)	ζ_X (0.48 ± 0.07) ζ_{RV} (0.5 ± 0.1)
12:14	ζ_X (1.04 ± 0.05) ζ_{RV} (1.18 ± 0.07)	ζ_X (0.48 ± 0.05) ζ_{RV} (0.48 ± 0.09)	ζ_X (0.8 ± 0.06) ζ_{RR} (0.83 ± 0.06)	λ_3 (0.93 ± 0.06) q_1 (0.92 ± 0.08)
12:29	λ_3 (1.02 ± 0.07) q_1 (0.89 ± 0.1)	λ_3 (0.6 ± 0.08) q_1 (0.56 ± 0.11)	λ_3 (0.69 ± 0.08) $\det\big(C_{(RR,RL)}\big)$ (0.63 ± 0.06)	λ_3 (0.8 ± 0.08) $\det\big(C_{(RH,RV)}\big)$ (0.81 ± 0.1)
13:03	ζ_X (1.09 ± 0.07) ζ_{RV} (1.15 ± 0.15)	ζ_X (0.42 ± 0.09) ζ_{RV} (0.39 ± 0.11)	ζ_X (0.66 ± 0.09) ζ_{RV} (0.61 ± 0.14)	λ_3 (0.8 ± 0.09) q_1 (0.7 ± 0.15)
13:18	λ_3 (1.28 ± 0.06) $\det\big(C_{(RH,RV)}\big)$ (1 ± 0.09)	μ_C (0.78 ± 0.32) $\phi_{(RH,RV)}$ (0.31 ± 0.36)	λ_3 (0.64 ± 0.07) q_1 (0.54 ± 0.08)	λ_3 (0.53 ± 0.07) q_1 (0.51 ± 0.03)

D. Polarimetric Features With the Highest Separability

The highest JM separability between the slicks and the open water regions (see Table VI) is provided by λ_3, ζ_{VV}, $\det(\boldsymbol{C}_{(\text{FP})})$, PD, $\text{span}(\boldsymbol{C}_{(\text{FP})})$, and ζ_X in FP. λ_3 is the feature that provides the highest JM separability most frequently. The majority of the mean JM is around 0.9–1.1, while the standard deviation is around 0.1, which indicates that the JM has a small variation within the open water subsets that are used. The best polarimetric FP features, i.e., λ_3, ζ_{VV}, $\det(\boldsymbol{C}_{(\text{FP})})$, and ζ_X, were also evaluated as a function of time. All showed a similar trend with time as in Fig. 11, but are left out due to space limitation. The best HP features to detect the various oil slicks are ζ_{RR}, ζ_{RV}, $\det(\boldsymbol{C}_{(\text{RH,RV})})$, $\det(\boldsymbol{C}_{(\text{RR,RL})})$, q_0, and q_1, and they all have a similar separability trend as a function of time to the best FP features. ζ_{RV} and ζ_{RR} are the HP features that provide the highest JM separability along the time series.

Overall, the best FP features are 0.6% better for detecting the E80 compared with the simulated HP features. For E60 and E40, the best FP features are 1.6% and 3.3% better than the HP features for detection. However, for the detection of the PO, the best HP features showed 0.8% better detection ability compared with the FP.

VII. CONCLUSION

A comparison between FP and simulated HP data from a UAVSAR time series of recently released and evolving oil slicks has been presented. The relative performance of FP and simulated HP in slick detection capability using a wide range of polarization-dependent features has been carefully evaluated using the JM separability.

Overall, the FP features were estimated to be 0%–3.3% better at distinguishing the various emulsion oil slicks from the ambient sea surface compared with the simulated HP features, while the best simulated HP features were 0.8% better than the FP features to distinguish the PO from the open water region. The best HP features show lower separability than the best FP features in the end of the $\sim$8 h time series compared with the beginning for the emulsion slicks. The FP features containing the cross-polarization scattering component are found to be best at distinguishing the various slicks from open water, and however, these cross-polarization features are not possible to isolate when using the HP mode. ζ_{RR}, ζ_{RV}, q_1, and q_0 are good alternatives to separate the slicks from the open water regions using the HP mode. High separability values between the oil slicks and the open water were also obtained using

$\det(\boldsymbol{C}_{(\mathrm{RH,RV})})$ and $\det(\boldsymbol{C}_{(\mathrm{RR,RL})})$, and their potential should be further investigated for other types of oil under various wind and ocean conditions. Overall, the best FP features are ζ_X, $\det(\boldsymbol{C}_{(\mathrm{FP})})$, λ_3, and ζ_{VV}.

This paper reveals a high correspondence between the results and the scattering theory of the two-scale Bragg model. All the features that showed poor detectability of the oil slicks are independent of the ocean wave spectrum (the small-scale roughness), while the features resulting in good separability were dependent, amongst other factor, on the ocean wave spectrum.

This paper highlights the importance of performing an incidence angle correction on the complex scattering vector prior to segmentation.

In general, the PO has the highest detectability across the full time series for both the FP and the HP modes, and its detectability does not decrease at the end of the UAVSAR time series, as is the case for the emulsion slicks. It was not possible to discriminate the PO from the emulsion slicks, which might be a result of the high wind and the relatively small volume of the released oils.

Our findings suggest that a similar slick-sea separability performance can be achieved using either HP or FP data at high wind conditions and for small slicks in volume. However, this paper should be repeated for data collected in other wind conditions and for various oil thicknesses. Further investigation should be conducted to determine whether real HP data could achieve the same results as both the FP and simulated HP data. Real HP data would reduce complexity (compared with the FP mode) of the sensor in terms of average power, on-board mass, and data volume, and provide more design flexibility.

APPENDIX
INCIDENCE ANGLE CORRECTION

The UAVSAR instrument images at incidence angles between 20° and 65° [5], and the ocean backscatter is known to decrease with increasing incidence angle. The oil slick regions in the UAVSAR time series are selected based on a segmentation method that is discussed in Section IV-C. The intensity variation related to incidence angle can be larger than the intensity difference between the classes, and hence, the oil slicks might be neglected in the original segmentation. Furthermore, the oil slicks spread out in the range direction with time, increasing the incidence angle span across the slicks. Hence, the effects from the incidence angle on the output regions are more significant in the last passes of the UAVSAR time series when the slicks have spread out. Therefore, to avoid the incidence angle effect dominating the segmentation, and to allow incidence angle independent comparison across the time series, an incidence angle correction is performed on the scattering vector prior to multilooking, segmentation, and feature computation. The incidence angle correction is obtained from the following expression [68]:

$$\boldsymbol{S}(\theta) = \boldsymbol{S'}\sqrt{\frac{\sin(\theta)}{\sin(\theta_{ref})}} \implies \boldsymbol{S'} = \boldsymbol{S}(\theta)\sqrt{\frac{1}{\gamma(\theta)}} \tag{22}$$

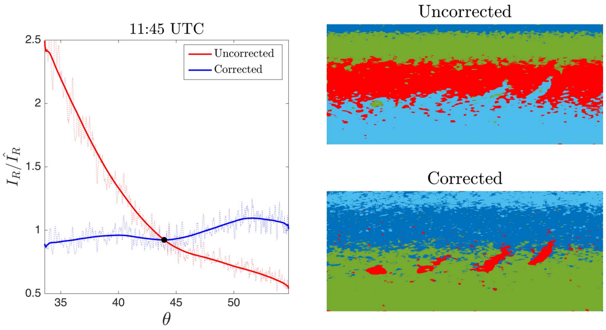

Fig. 12. Illustration of the incidence angle correction applied to the UAVSAR scene acquired at 11:45 UTC. (Left) Smoothed mean VV-intensity profiles normalized to the mean of the span profile using the clean sea region before (red line) and after correction (blue line). Dotted lines: unsmoothed mean intensity profiles. Black marker: reference level, i.e., the mean of the span along the range direction. (Right) Results of the segmentation with and without incidence angle correction. Colors: various output segments.

where $\boldsymbol{S}(\theta)$ is the measured scattering vector dependent on the incidence angle, θ is the incidence angle, θ_{ref} is the reference angle, $\boldsymbol{S'}$ is the corrected scattering vector independent of the incidence angle, and $\gamma(\theta)$ is the $((\sin(\theta))/(\sin(\theta_{\mathrm{ref}})))$ fraction. Because we are dealing with the complex scattering vector, rather than intensities, the square root is applied. Range and incidence angle are related in a one-to-one correspondence, and hence, $\gamma(r)$ rather than $\gamma(\theta)$ is used.

To preserve the polarimetry in the data, the same $\gamma(r)$ value should be used when correcting the different complex scattering components, i.e., S_{HH}, S_{HV}, and S_{VV}. Selecting different $\gamma(r)$ values for each complex scattering component could influence the various multivariate polarimetric features, such as the determinant of the covariance matrix. Rather than determining the relation between range and incidence angle, we estimate $\gamma(r)$ empirically from the span of the intensities ($\mathrm{span} = I_{\mathrm{HH}} + I_{\mathrm{VV}} + I_{\mathrm{HV}}$) by considering a region of clean water (no ships nor oil slicks), and assuming that this region is homogenous and has no texture. For this paper, the region along the range direction was selected from the span, and contained 1000 pixels in the azimuth direction. An intensity profile ($I_{\mathrm{Rg}}^{\mathrm{span}}$) from the span was created by taking the average of that region, and these values were further smoothed in the range direction. The reference level was chosen to be the mean value of the total power along the range direction ($\hat{I}_{\mathrm{Rg}}^{\mathrm{span}}$). $\gamma(r)$ can be estimated as

$$\gamma(r) \approx \frac{I_{Rg}^{\mathrm{span}}}{\hat{I}_{Rg}^{\mathrm{span}}}. \tag{23}$$

Fig. 12 shows the incidence angle correction applied to an ascending UAVSAR scene. The blue line is the corrected smoothed mean VV-intensity along the range direction (normalized to the mean intensity value), and the dashed blue line is the unsmoothed corrected mean intensity value along the range direction, also normalized. Here, we use the incidence angle (covering the location of the oil slicks) on the x-axes. The red line is the smoothed uncorrected mean VV-intensity profile, and the dashed red line is the unsmoothed version of that profile. Only the VV-intensity is used to demonstrate this, but the same behavior was observed for the

HH and HV intensities. After applying this correction method, the incidence angle dependence of the scattering components is reduced.

The corrected intensity profile is not a perfectly flat curve in any of the individual channels, which might be because they are corrected based on span, and the visible polarimetric variation indicates that there is some local variations.

From visual inspection of the right panel in Fig. 12, it is clear that the intensities are significantly affected by the incidence angle. One example of how the incidence angle effects the segmentation results is also shown in Fig. 12. Here, the top-right figure displays the results of the segmentation using uncorrected data as input, while the bottom-right image is when the incidence angle correction is applied prior to the segmentation method. Clearly, the segmentation method did not successfully locate the oil slicks in the uncorrected case. However, if the corrected data are used, the segmentation algorithm successfully identifies the oil slicks. These segmentation results highlight how important it is to perform the incidence angle correction prior to segmentation. This correction is done on all the UAVSAR scenes prior to segmentation and feature computation.

Calculating the intensity values from the corrected scattering vector yields an approximation of the damping ratio. This is because the entire intensity image is normalized using the mean of a chosen open water region ($I_{\mathrm{Rg}}^{\mathrm{span}}$). The corrected intensities are named damping ratios (see Tables III and V), and are labeled ζ, for example

$$\zeta_{\mathrm{VV}} = \left\langle \left| S'_{\mathrm{VV}} \right|^2 \right\rangle \tag{24}$$

where $\langle\cdot\rangle$ represents the averaging (multilooking).

ACKNOWLEDGMENT

The authors would like to thank NOFO for hosting NORSE2015 and MET Norway for collecting the meteorological and ocean observations. They would also like to thank the reviewers for their useful comments and suggestions. UAVSAR data are the courtesy of NASA/JPL Caltech.

REFERENCES

[1] B. Minchew, C. E. Jones, and B. Holt, "Polarimetric analysis of backscatter from the deepwater horizon oil spill using L-band synthetic aperture radar," *IEEE Trans. Geosci. Remote Sens.*, vol. 50, no. 10, pp. 3812–3830, Oct. 2012.

[2] S. Skrunes, C. Brekke, and T. Eltoft, "Characterization of marine surface slicks by Radarsat-2 multipolarization features," *IEEE Trans. Geosci. Remote Sens.*, vol. 52, no. 9, pp. 5302–5319, Sep. 2014.

[3] S. Skrunes, C. Brekke, T. Eltoft, and V. Kudryavtsev, "Comparing near-coincident C- and X-band SAR acquisitions of marine oil spills," *IEEE Trans. Geosci. Remote Sens.*, vol. 53, no. 4, pp. 1958–1975, Apr. 2015.

[4] M. Migliaccio, F. Nunziata, and A. Gambardella, "On the co-polarized phase difference for oil spill observation," *Int. J. Remote Sens.*, vol. 30, no. 6, pp. 1589–1602, Mar. 2009.

[5] A. G. Fore *et al.*, "UAVSAR polarimetric calibration," *IEEE Trans. Geosci. Remote Sens.*, vol. 53, no. 6, pp. 3481–3491, Jun. 2015.

[6] R. K. Raney, "Hybrid-polarity SAR architecture," *IEEE Trans. Geosci. Remote Sens.*, vol. 45, no. 11, pp. 3397–3404, Nov. 2007.

[7] F. J. Charbonneau *et al.*, "Compact polarimetry overview and applications assessment," *Can. J. Remote Sens.*, vol. 36, no. S2, pp. S298–S315, 2010.

[8] J.-C. Souyris, P. Imboa, R. Fjørtoft, S. Mingot, and J.-S. Lee, "Compact polarimetry based on symmetry properties of geophysical media: The $\pi/4$ mode," *IEEE Trans. Geosci. Remote Sens.*, vol. 43, no. 3, pp. 634–646, Mar. 2005.

[9] F. Nunziata, M. Migliaccio, and X. Li, "Sea oil slick observation using hybrid-polarity SAR architecture," *IEEE J. Ocean. Eng.*, vol. 40, no. 2, pp. 426–440, Apr. 2015.

[10] A.-B. Salberg, O. Rudjord, and A. H. S. Solberg, "Oil spill detection in hybrid-polarimetric SAR images," *IEEE Trans. Geosci. Remote Sens.*, vol. 52, no. 10, pp. 6521–6533, Oct. 2014.

[11] M. J. Collins, M. Denbina, B. Minchew, C. E. Jones, and B. Holt, "On the use of simulated airborne compact polarimetric SAR for characterizing oil–water mixing of the deepwater horizon oil spill," *IEEE J. Sel. Topics Appl. Earth Observat. Remote Sens.*, vol. 8, no. 3, pp. 1062–1077, Mar. 2015.

[12] R. Shirvany, M. Chabert, and J.-Y. Tourneret, "Ship and oil-spill detection using the degree of polarization in linear and hybrid/compact dual-pol SAR," *IEEE J. Sel. Topics Appl. Earth Observat. Remote Sens.*, vol. 5, no. 3, pp. 885–892, Jun. 2012.

[13] B. Minchew, "Determining the mixing of oil and sea water using polarimetric synthetic aperture radar," *Geophys. Res. Lett.*, vol. 39, no. 16, Aug. 2012.

[14] W. Alpers and H. Hühnerfuss, "Radar signatures of oil films floating on the sea surface and the Marangoni effect," *J. Geophys. Res.*, vol. 93, no. C4, pp. 3642–3648, Apr. 1988.

[15] G. R. Valenzuela, "Theories for the interaction of electromagnetic and oceanic waves—A review," *Boundary-Layer Meteorol.*, vol. 13, no. 1, pp. 61–85, Jan. 1978.

[16] B. Holt, "SAR imaging of the ocean surface," in *Synthetic Aperture Radar Marine User's Manual*, C. R. Jackson and J. R. Apel, Eds. Washington, DC, USA: NOAA NESDIS Office of Research and Applications, 2004, pp. 25–79

[17] R. Romeiser, V. Wismann, and W. Alpers, "An improved composite surface model for the radar backscattering cross section of the ocean surface: 1. Theory of the model and optimization/validation by scatterometer data," *J. Geophys. Res.*, vol. 102, no. C11, pp. 25237–25250, Nov. 1997.

[18] C. Brekke, C. E. Jones, S. Skrunes, B. Holt, M. Espeseth, and T. Eltoft, "Cross-correlation between polarization channels in SAR imagery over oceanographic features," *IEEE Geosci. Remote Sens. Lett.*, vol. 13, no. 7, pp. 997–1001, Jul. 2016.

[19] S. Skrunes, C. Brekke, C. E. Jones, and B. Holt, "A multisensor comparison of experimental oil spills in polarimetric SAR for high wind conditions," *IEEE J. Sel. Topics Appl. Earth Observat. Remote Sens.*, vol. 9, no. 11, pp. 4948–4961, Nov. 2016.

[20] C. E. Jones *et al.*, "Measurement and modeling of oil slick transport," *J. Geophys. Res. Oceans*, vol. 121, no. 10, pp. 7759—7775, 2016.

[21] M. E. Nord, T. L. Ainsworth, J.-S. Lee, and N. J. S. Stacy, "Comparison of compact polarimetric synthetic aperture radar modes," *IEEE Trans. Geosci. Remote Sens.*, vol. 47, no. 1, pp. 174–188, Jan. 2008.

[22] S. R. Cloude, *Polarisation Applications in Remote Sensing*, 1st, ed. Oxford, U.K.: Oxford Univ. Press, 2010.

[23] R. K. Raney, "A perspective on compact polarimetry," *IEEE Geosci. Remote Sens. Newslett.*, no. 160, pp. 12–18, Sep. 2010.

[24] M. J. Collins, M. Denbina, and G. Atteia, "On the reconstruction of quad-Pol SAR data from compact polarimetry data for ocean target detection," *IEEE Trans. Geosci. Remote Sens.*, vol. 51, no. 1, pp. 591–600, Jan. 2013.

[25] R. K. Raney, "Comparing compact and quadrature polarimetric SAR performance," *IEEE Geosci. Remote Sens. Lett.*, vol. 13, no. 6, pp. 861–864, Jun. 2016.

[26] A. Iodice, A. Natale, and D. Riccio, "Retrieval of soil surface parameters via a polarimetric two-scale model," *IEEE Trans. Geosci. Remote Sens.*, vol. 49, no. 7, pp. 2531–2547, Jul. 2011.

[27] J.-S. Lee, D. L. Schuler, and T. L. Ainsworth, "Polarimetric SAR Data Compensation for Terrain Azimuth Slope Variation," *IEEE Trans. Geosci. Remote Sens.*, vol. 38, no. 5, pp. 2153–2163, Sep. 2000.

[28] M. M. Espeseth, S. Skrunes, C. Brekke, A.-B. Salberg, C. E. Jones, and B. Holt, "Oil spill characterization in the hybrid polarity SAR domain using log-cumulants," *Proc. SPIE*, vol. 10004, p. 1000414, Oct. 2016.

[29] C. E. Jones, M. M. Espeseth, B. Holt, C. Brekke, and S. Skrunes, "Characterization and discrimination of evolving mineral and plant oil slicks based on L-band synthetic aperture radar (SAR)," *Proc. SPIE*, vol. 10003, p. 100030K, Oct. 2016.

[30] M. Basseville, "Distance measures for signal processing and pattern recognition," *Signal Process.*, vol. 18, no. 4, pp. 349–369, 1989.

[31] Y. Li, H. Lin, Y. Zhang, and J. Chen, "Comparisons of circular transmit and linear receive compact polarimetric SAR features for oil slicks discrimination," *J. Sensors*, vol. 2015, 2015, Art. no. 631561.

[32] M. Migliaccio, A. Gambardella, and M. Tranfaglia, "SAR polarimetry to observe oil spills," *IEEE Trans. Geosci. Remote Sens.*, vol. 45, no. 2, pp. 506–511, Feb. 2007.

[33] M. Dabbor, S. Howell, M. Shokr, and J. Yackel, "The Jeffries–Matusita distance for the case of complex Wishart distribution as a separability criterion for fully polarimetric SAR data," *Int. J. Remote Sens.*, vol. 35, no. 19, pp. 6859–6873, Oct. 2014.

[34] P. H. Swain and S. M. Davis, *Remote Sensing: The Quantitative Approach*. New York, NY, USA: McGraw-Hill, 1978.

[35] M. Dabboor and T. Geldsetzer, "On the classification of sea ice types using simulated radarsat constellation mission (RCM) compact polarimetric SAR parameters," in *Proc. ASPRS Annu. Conf.*, Louisville, KY, USA, Mar. 2014.

[36] M. Migliaccio, M. Tranfaglia, and S. A. Ermakov, "A physical approach for the observation of oil spills in SAR images," *IEEE J. Ocean. Eng.*, vol. 30, no. 3, pp. 496–507, Jul. 2005.

[37] F. Galland, P. Réfrégier, and O. Germain, "Synthetic aperture radar oil spill segmentation by stochastic complexity minimization," *IEEE Geosci. Remote Sens. Lett.*, vol. 1, no. 4, pp. 295–299, Oct. 2014.

[38] S. Derrode and G. Mercier, "Unsupervised multiscale oil slick segmentation from SAR images using a vector HMC model," *Pattern Recognit.*, vol. 40, no. 3, pp. 1135–1147, Mar. 2007.

[39] A. P. Doulgeris and T. Eltoft, "Scale mixture of Gaussian modelling of polarimetric SAR data," *EURASIP J. Adv. Signal Process.*, vol. 2010, p. 12, Dec. 2009.

[40] A. P. Doulgeris, "A simple and extendable segmentation method for multi-polarisation SAR images," in *Proc. POLINSAR*, Frascati, Italy, 2013.

[41] V. Wismann, M. Gade, W. Alpers, and H. Huhnerfuss, "Radar signatures of marine mineral oil spills measured by an airborne multi-frequency radar," *Int. J. Remote Sens.*, vol. 19, no. 18, pp. 3607–3623, 1998.

[42] N. Pinel, C. Bourlier, and I. Sergievskaya, "Two-dimensional radar backscattering modeling of oil slicks at sea based on the model of local balance: Validation of two asymptotic techniques for thick films," *IEEE Trans. Geosci. Remote Sens.*, vol. 52, no. 5, pp. 2326–2338, May 2014.

[43] D. L. Schuler, J.-S. Lee, and K. W. Hoppel, "Polarimetric SAR image signatures of the ocean and Gulf Stream features," *IEEE Trans. Geosci. Remote Sens.*, vol. 31, no. 6, pp. 1210–1221, Nov. 1993.

[44] D. Velotto, M. Migliaccio, F. Nunziata, and S. Lehner, "Dual-polarized TerraSAR-X data for oil-spill observation," *IEEE Trans. Geosci. Remote Sens.*, vol. 49, no. 12, pp. 4751–4762, Dec. 2011.

[45] W. Wenguang, L. Fei, W. Peng, and W. Jun, "Oil spill detection from polarimetric SAR image," in *Proc. ICSP*, 2010, pp. 823–835.

[46] B. Zhang, W. Perrie, X. Li, and W. G. Pichel, "Mapping sea surface oil slicks using RADARSAT-2 quad-polarization SAR image," *Geophys. Res. Lett.*, vol. 38, no. 10, May 2011.

[47] V. N. Kudryavtsev, B. Chapron, A. G. Myasoedov, F. Collard, and J. A. Johannessen, "On dual co-polarized SAR measurements of the ocean surface," *IEEE Geosci. Remote Sens. Lett.*, vol. 10, no. 4, pp. 761–765, Jul. 2013.

[48] W. Tian, Y. Shao, J. Yuan, S. Wang, and Y. Liu, "An experiment for oil spill recognition using RADARSAT-2 image," in *Proc. IEEE Int. Geosci. Remote Sens. Symp.*, Jul. 2010, pp. 2761–2764.

[49] M. Migliaccioa, F. Nunziata, and A. Buono, "SAR polarimetry for sea oil slick observation," *Int. J. Remote Sens.*, vol. 36, no. 12, pp. 3243–3273, Jun. 2015.

[50] D. L. Schuler and J. S. Lee, "Mapping ocean surface features using biogenic slick-fields and SAR polarimetric decomposition techniques," *IEE Proc.-Radar, Sonar Navigat.*, vol. 153, no. 3, pp. 260–270, Jun. 2006.

[51] M. Migliaccio, A. Gambardella, F. Nunziata, M. Shimada, and O. Isoguchi, "The PALSAR polarimetric mode for sea oil slick observation," *IEEE Trans. Geosci. Remote Sens.*, vol. 47, no. 12, pp. 4032–4041, Dec. 2009.

[52] F. T. Ulaby, K. Sarabandi, and A. Nashashibi, "Statistical properties of the Müller matrix of distributed targets," *IEE Proc. F-Radar Signal Process.*, vol. 139, no. 2, pp. 136–146, Apr. 1992.

[53] M. R. Drinkwater, R. Kwok, E. Rignot, H. Israelsson, R. G. Onstott, and D. P. Winebrenner, "Potential applications of polarimetry to the classification of sea ice," in *Microwave Remote Sensing of Sea Ice* (Geophysical Monograph). Washington, DC, USA: Amer. Geophys. Union, 1992.

[54] J.-S. Lee and E. Pottier, *Polarimetric Radar Imaging, From Basics to Applications*, B. J. Thompson, Ed. Boca Raton, FL, USA: CRC Press, 2009.

[55] H. Li, W. Perrie, Y. Zhou, and Y. He, "Oil spill detection on the ocean surface using hybrid polarimetric SAR imagery," *Sci. China*, vol. 59, no. 2, pp. 249–257, Feb. 2016.

[56] H. Li, W. Perrie, Y. He, J. Wu, and X. Luo, "Analysis of the polarimetric SAR scattering properties of oil-covered waters," *IEEE J. Sel. Topics Appl. Earth Observat. Remote Sens.*, vol. 8, no. 8, pp. 3751–3759, Aug. 2015.

[57] S. Cloude, D. Goodenough, and H. Chen, "Compact decomposition theory," *IEEE Trans. Geosci. Remote Sens.*, vol. 9, no. 1, pp. 28–32, Jan. 2012.

[58] R. K. Raney, J. T. S. Cahill, G. W. Patterson, and D. B. J. Bussey, "The $m - chi$ decomposition of hybrid dual-polarimetric radar data with application to lunar craters," *J. Geophys. Res.*, vol. 117, no. E12, May 2012.

[59] B. Slade, *Radarsat-2 Product Description*. Rickmond, BC, Canada: MacDonald, Dettwiler Assoc., 2011.

[60] T. Fritz and M. Eineder, "TerraSAR-X ground segment basic product specification document," German Aerosp. Center Abbreviated DLR, DLR, Germany, Tech. Rep., Oct. 2010. [Online]. Available: http://www.dtic.mil/dtic/tr/fulltext/u2/a515513.pdf

[61] D. Latini, F. D. Frate, and C. E. Jones, "Multi-frequency and polarimetric quantitative analysis of the Gulf of Mexico oil spill event comparing different SAR systems," *Remote Sens. Environ.*, vol. 183, pp. 26–42, Sep. 2016.

[62] T. Misra *et al.*, "Synthetic aperture radar payload on-board RISAT-1: Configuration, technology and performance," *Current Sci.*, vol. 104, no. 4, pp. 446–461, Feb. 2013.

[63] S. Skrunes, C. E. Jones, C. Brekke, B. Holt, and M. M. Espeseth, "On the effects of imaging geometry on multipolarization SAR features for oil spill observation," in *Proc. Living Planet Symp.*, 2016, p. 72.

[64] R. Shirvany, M. Chabert, and J. Y. Tourneret, "Estimation of the degree of polarization for hybrid/compact and linear dual-pol SAR intensity images: Principles and applications," *IEEE Trans. Geosci. Remote Sens.*, vol. 51, no. 1, pp. 539–551, Jan. 2013.

[65] A. H. S. Solberg, "Remote sensing of ocean oil-spill pollution," *Proc. IEEE*, vol. 100, no. 10, pp. 2931–2945, Oct. 2012.

[66] J. Coleman, *Oil Sea III*. Washington, DC, USA: Nat. Acad. Press, 2003.

[67] W. Alpers and H. A. Espedal, "Oils and surfactants," in *Synthetic Aperture Radar Marine User's Manual*, C. R. Jackson and J. R. Apel, Eds. Washington, DC, USA: NOAA NESDIS Office of Research and Applications, 2004, pp. 263–275

[68] G. Sun, K. J. Ranson, and V. I. Kharuk, "Radiometric slope correction for forest biomass estimation from SAR data in Western Sayani Mountains, Siberia," *Remote Sens. Env.*, vol. 79, nos. 2–3, pp. 279–287, 2002.

Martine M. Espeseth received the M.Sc. degree from the UiT The Arctic University of Norway, Tromsø, Norway, in 2015, where she is currently pursuing the Ph.D. degree with the Centre for Integrated Remote Sensing and Forecasting for Arctic Operations.

In 2016, she was a Visiting Ph.D. Student with the Jet Propulsion Laboratory, California Institute of Technology, Pasadena, CA, USA. Her research interests include remote sensing of polarimetric synthetic aperture radar and with a focus on compact polarimetry within both marine oil pollution and sea ice applications.

Stine Skrunes (S'12–M'15) received the M.Sc. and Ph.D. degrees from the UiT The Arctic University of Norway, Tromsø, Norway, in 2011 and 2014, respectively.

She holds a post-doctoral position with the Department of Physics and Technology, Centre for Integrated Remote Sensing and Forecasting for Arctic Operations, UiT The Arctic University of Norway. Her research interests include remote sensing of ocean areas, specifically by polarimetric synthetic aperture radar and with a focus on marine oil pollution.

Cathleen E. Jones (M'94) received the B.S. degree in physics from Texas A&M University, College Station, TX, USA, and the Ph.D. degree in physics from the California Institute of Technology, Pasadena, CA, USA.

She is currently a Radar Scientist with the NASA's Jet Propulsion Laboratory, California Institute of Technology, where she is involved in using radar remote sensing for studying natural disasters and monitoring critical infrastructure, primarily using high-resolution L-band PolSAR and InSAR based on UAVSAR data. Her research interests include the development of methods for determining oil slick characteristics and identifying levee deformation, seepage, and general subsidence rates using synthetic aperture radar, and detecting sinkhole precursor in InSAR-challenged areas.

Camilla Brekke (M'12) received the Cand.Sci. and Ph.D. degrees from the University of Oslo, Oslo, Norway, in 2001 and 2008, respectively.

In 2001, she was a System Developer with Ericsson, Asker, Norway. From 2001 to 2002, she was a Young Graduate Trainee with the European Space Agency, Noordwijk, The Netherlands. From 2002 to 2009, she was a Scientist with the Norwegian Defense Research Establishment, Kjeller, Norway. In 2009, she joined the Department of Physics and Technology, UiT The Arctic University of Norway, Tromsø, Norway, as an Associate Professor. From 2012 to 2013, she was a Visiting Scientist with the Jet Propulsion Laboratory, California Institute of Technology, Pasadena, CA, USA. She is currently with the Earth Observation Laboratory and the Centre for Integrated Remote Sensing and Forecasting for Arctic Operations, UiT The Arctic University of Norway. Her research interests include signal and image processing of synthetic aperture radar data for arctic and marine applications.

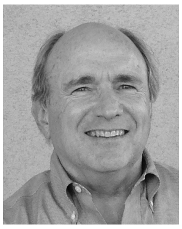

Benjamin Holt (M'88) received the B.S. degree from Stanford University, Stanford, CA, USA, in 1972, and the M.S. degree in physical oceanography from the University of Southern California, Los Angeles, CA, USA, in 1988.

In 1978, he joined the California Institute of Technology, Pasadena, CA, USA, where he is currently a Research Scientist with the Jet Propulsion Laboratory, Ocean Circulation Group, Earth Science Section. His research interests include using multisensor remote sensing data to examine the geophysical state of polar sea ice and snow, coastal oceanography and circulation, and the detection of marine pollutants, and new instrument development and techniques for microwave measurement of sea ice thickness.

Anthony P. Doulgeris (S'06–M'12) received the B.Sc. degree in physics from The Australian National University, Canberra, ACT, Australia, in 1988, and the M.Sc. and Ph.D. degrees in physics from the UiT The Arctic University of Norway, Tromsø, Norway, in 2006 and 2011, respectively.

He joined the Department of Physics and Technology, UiT The Arctic University of Norway, in 2007. He is currently an Associate Professor in applied Earth observation. His research interests include investigating remote sensing, pattern recognition, and multidimensional statistical modeling, in particular with polarimetric synthetic aperture radar images.